



NAVAL POSTGRADUATE SCHOOL

MONTEREY, CALIFORNIA

THESIS

**NOVEL SYNTHESIS AND CHARACTERIZATION
OF INORGANIC FULLERENE TYPE WS₂ AND
GRAPHENE HYBRIDS**

by

Ashley R. Maxson

March 2013

Thesis Advisor:
Second Reader:

Claudia C. Luhrs
Luke N. Brewer

Approved for public release; distribution is unlimited

THIS PAGE INTENTIONALLY LEFT BLANK

REPORT DOCUMENTATION PAGE			<i>Form Approved OMB No. 0704-0188</i>	
Public reporting burden for this collection of information is estimated to average 1 hour per response, including the time for reviewing instruction, searching existing data sources, gathering and maintaining the data needed, and completing and reviewing the collection of information. Send comments regarding this burden estimate or any other aspect of this collection of information, including suggestions for reducing this burden, to Washington headquarters Services, Directorate for Information Operations and Reports, 1215 Jefferson Davis Highway, Suite 1204, Arlington, VA 22202-4302, and to the Office of Management and Budget, Paperwork Reduction Project (0704-0188) Washington, DC 20503.				
1. AGENCY USE ONLY (Leave blank)		2. REPORT DATE March 2013	3. REPORT TYPE AND DATES COVERED Master's Thesis	
4. TITLE AND SUBTITLE NOVEL SYNTHESIS AND CHARACTERIZATION OF INORGANIC FULLERENE TYPE WS2 AND GRAPHENE HYBRIDS			5. FUNDING NUMBERS RMF5Y	
6. AUTHOR(S) Ashley R. Maxson				
7. PERFORMING ORGANIZATION NAME(S) AND ADDRESS(ES) Naval Postgraduate School Monterey, CA 93943-5000			8. PERFORMING ORGANIZATION REPORT NUMBER	
9. SPONSORING /MONITORING AGENCY NAME(S) AND ADDRESS(ES) N/A			10. SPONSORING/MONITORING AGENCY REPORT NUMBER	
11. SUPPLEMENTARY NOTES The views expressed in this thesis are those of the author and do not reflect the official policy or position of the Department of Defense or the U.S. Government. IRB Protocol number ____N/A____.				
12a. DISTRIBUTION / AVAILABILITY STATEMENT Approved for public release; distribution is unlimited			12b. DISTRIBUTION CODE A	
13. ABSTRACT (maximum 200 words) <p>With the aim to develop personal protection systems with improved mechanical properties and reduced weight, this research combined graphene with tungsten disulfide, and studied this hybrid system included in epoxy resin. A novel plasma production process generated nanometric size tungsten oxide (WO₃) spherical particles. The nanospheres were sulfurized to produce inorganic-fullerene type tungsten disulfide (IF-WS₂). The plasma IF-WS₂ particles exhibited smaller particle size, characteristic hollow cores and larger angle facets than IF-WS₂ from commercial WO₃, and morphological characteristics that are correlated with improved mechanical properties.</p> <p>Exfoliated graphene sheets were prepared from graphite nanopowder through oxidization and subsequent exfoliation at 800°C in inert atmosphere.</p> <p>Sample microstructures were characterized by XRD, SEM, TEM and FIB.</p> <p>Protocols to fabricate hybrid graphene/IF-WS₂ with nanoscale dispersions were developed. Hybrids from <i>in-situ</i> routes and physical mixtures of individual components were included in epoxy matrices for nanoindentation tests. Results showed the Young's modulus (normalized for bare epoxy) increased 12.23%, while hardness increased 27.87% through inclusion of 1% wt loadings of graphene/IF-WS₂. These results were compared to carbon nanofibers/IF-WS₂ hybrid composites recently produced by the functional materials research group at NPS. This research represents a step toward development of lightweight nano-architectures for advanced personal protection systems.</p>				
14. SUBJECT TERMS Graphene, IF-WS2, Epoxy Composites, Personal Protection Systems			15. NUMBER OF PAGES 101	
			16. PRICE CODE	
17. SECURITY CLASSIFICATION OF REPORT Unclassified	18. SECURITY CLASSIFICATION OF THIS PAGE Unclassified	19. SECURITY CLASSIFICATION OF ABSTRACT Unclassified	20. LIMITATION OF ABSTRACT UU	

THIS PAGE INTENTIONALLY LEFT BLANK

Approved for public release; distribution is unlimited

**NOVEL SYNTHESIS AND CHARACTERIZATION
OF INORGANIC FULLERENE TYPE WS₂ AND GRAPHENE HYBRIDS**

Ashley R. Maxson
Lieutenant, United States Navy
B.S., United States Naval Academy, 2004

Submitted in partial fulfillment of the
requirements for the degree of

MASTER OF SCIENCE IN MECHANICAL ENGINEERING

from the

**NAVAL POSTGRADUATE SCHOOL
March 2013**

Author: Ashley R. Maxson

Approved by: Claudia C. Luhrs
Thesis Advisor

Luke N. Brewer
Second Reader

Knox T. Millsaps
Chair, Department of Mechanical and Aerospace Engineering

THIS PAGE INTENTIONALLY LEFT BLANK

ABSTRACT

With the aim to develop personal protection systems with improved mechanical properties and reduced weight, this research combined graphene with tungsten disulfide, and studied this hybrid system included in epoxy resin.

A novel plasma production process generated nanometric size tungsten oxide (WO_3) spherical particles. The nanospheres were sulfurized to produce inorganic-fullerene type tungsten disulfide (IF- WS_2). The plasma IF- WS_2 particles exhibited smaller particle size, characteristic hollow cores and larger angle facets than IF- WS_2 from commercial WO_3 , and morphological characteristics that are correlated with improved mechanical properties.

Exfoliated graphene sheets were prepared from graphite nanopowder through oxidization and subsequent exfoliation at 800°C in inert atmosphere.

Sample microstructures were characterized by XRD, SEM, TEM and FIB.

Protocols to fabricate hybrid graphene/IF- WS_2 with nanoscale dispersions were developed. Hybrids from *in-situ* routes and physical mixtures of individual components were included in epoxy matrices for nanoindentation tests. Results showed the Young's modulus (normalized for bare epoxy) increased 12.23%, while hardness increased 27.87% through inclusion of 1% wt loadings of graphene/IF- WS_2 . These results were compared to carbon nanofibers/IF- WS_2 hybrid composites recently produced by the functional materials research group at NPS. This research represents a step toward development of lightweight nano-architectures for advanced personal protection systems.

THIS PAGE INTENTIONALLY LEFT BLANK

TABLE OF CONTENTS

I.	INTRODUCTION.....	1
A.	Overview	1
B.	Advances in Personal Protection Systems	1
C.	Graphene as Component.....	3
D.	Tungsten Disulfide Structures	4
E.	Thesis Objectives.....	7
F.	Hypothesis.....	8
G.	Naval Relevance of the Topic.....	8
II.	EXPERIMENTAL METHODS	9
A.	Synthesis Of Individual Component Nanoparticles.....	9
1.	Graphite Oxide Production.....	9
2.	Thermally Exfoliated Graphite Oxide (TEGO) Production	12
3.	Inorganic Fullerene Type WS ₂ Production	13
a.	From Ammonium Tetrathiotungstate Salts	13
b.	From Plasma Generated Tungsten Oxide.....	14
c.	From Commercial Tungsten Oxide Particles	15
B.	Fabrication of Hybrid Composite Graphene/IF-WS ₂	16
1.	In-Situ Production of Graphene/IF-WS ₂	17
2.	Physical Mixture of WS ₂ with Graphene.....	19
C.	Generation of Epoxy Resin Composites.....	19
III.	CHARACTERIZATION	23
A.	X-Ray Diffraction.....	23
B.	Transmission Electron Microscopy	25
C.	Scanning Electron Microscopy	26
D.	Energy-Dispersive Spectroscopy	27
E.	Focused Ion-Beam Milling	27
F.	Nanoindentation	28
IV.	RESULTS AND DISCUSSION	31
A.	Individual Components	31
1.	Commercial Graphite Nanopowder to GO to TEGO	31
2.	IF-WS ₂	37
a.	WS ₂ from Ammonium Tetrathiotungstate Salts	39
b.	WS ₂ from WO ₃ Commercial	40
c.	WS ₂ from WO ₃ Plasma	45
B.	Hybrid IF-WS ₂ and Graphene.....	58
1.	In-Situ Hybrid IF-WS ₂ and Graphene.....	59
a.	In-Situ Hybrid from (NH ₄) ₂ WS ₄ and TEGO.....	59
b.	In-Situ Hybrid from IF-WS ₂ Plasma and TEGO	60
2.	Physical Mixture Hybrid IF-WS ₂ and Graphene	62
3.	Nanoindentation	65

V.	CONCLUSIONS	73
A.	Milestones	73
B.	Next Steps	74
	LIST OF REFERENCES	77
	INITIAL DISTRIBUTION LIST	81

LIST OF FIGURES

Figure 1.	Photograph of two sailors wearing a “light” version of body armor (Image used with permission from LT Melanie Chambers and LT Kathryn Johnson).	2
Figure 2.	Graphic representing the 2D structure of graphene [13].	4
Figure 3.	Transmission Electron Microscope image of IF-WS ₂ showing the inorganic fullerene structure the brighter core is evidence of a hollow interior.	7
Figure 4.	Stepwise production of Graphite Oxide.	10
Figure 5.	Left) Branson Ultrasonic Sonicator Middle) Corning Hotplate and Stirrer Right) Hermle Z300 Centrifuge with 4x50 mL Rotor.	12
Figure 6.	Left) Mixture of Graphite Powder with Acids and KMnO ₄ and H ₂ O ₂ at the end of the Reaction Time Middle) GO prior to being placed under vacuum Right) Nalgene Vacuum Desiccator with Graphite Oxide Drying. .	12
Figure 7.	Left) Thermo Scientific Lindberg Blue M Tubular Furnace Middle) mks Multi Gas Controller 647C. Right) Mattheson E100 Flowmeter for Hydrogen Sulfide.	13
Figure 8.	Stepwise production of TEGO from GO.	13
Figure 9.	Stepwise production of WS ₂ from (NH ₄) ₂ WS ₄	14
Figure 10.	Aslex Atmospheric Microwave Plasma System used to create WO ₃	14
Figure 11.	Stepwise procedure for producing Plasma IF-WS ₂ from (NH ₄) ₂ WS ₄	15
Figure 12.	Stepwise procedure for production of WS ₂ from commercial WO ₃	16
Figure 13.	Stepwise procedure for in-situ non-sulfurized composite.	17
Figure 14.	Stepwise procedure for first in-situ sulfurized composite.	17
Figure 15.	Stepwise procedure for non-sulfurized composite from plasma WO ₃	18
Figure 16.	Stepwise procedure for sulfurized composite from WO ₃ plasma.	19
Figure 17.	Stepwise procedure for physical mixture of sulfurized composite.	19
Figure 18.	Struers Speci-Fix 20 Kit used to create epoxy mounts.	20
Figure 19.	Top) Silicone molds with 1% nanomaterials loading in the epoxy Middle) Epoxy mounts removed from the molds (center being neat and outer two with 1% loading). Bottom) Highly polished surface of epoxy mounts in tray of nanoindenter.	21
Figure 20.	Image of X-ray diffractometer.	25
Figure 21.	An image of the Zeiss SEM used to capture surface images of the samples..	26
Figure 22.	Agilent Technologies Nano Indenter G200 used for characterization via nanoindentation.	30
Figure 23.	Left) X-ray spectra for GO made from graphite nanopowder Right) Chemical peaks for GO made from graphite flakes, showing silicon impurities.	32
Figure 24.	SEM image of Commercial Graphite Nanopowder.	33
Figure 25.	Top) XRD graph for commercial graphite nanopowder Middle) XRD graph for GO Bottom) XRD graph for TEGO.	35
Figure 26.	SEM image of graphite oxide.	36

Figure 27.	SEM image of Thermally Exfoliated Graphite Oxide.	37
Figure 28.	XRD graph of WS ₂ from salts.	39
Figure 29.	Left) SEM image of WS ₂ from (NH ₄) ₂ WS ₄ Right) SEM image of WS ₂ from (NH ₄) ₂ WS ₄	40
Figure 30.	XRD graph for WO ₃ commercial.	41
Figure 31.	SEM image of hand crushed WO ₃ commercial.	42
Figure 32.	XRD graph of WS ₂ from WO ₃ commercial that shows the presence of WO ₃ after sulfurization.	43
Figure 33.	SEM image for WS ₂ from WO ₃ commercial.	44
Figure 34.	Histogram for particle size distribution for WS ₂ from WO ₃ commercial.	44
Figure 35.	XRD graphs of WO ₃ from plasma.	47
Figure 36.	SEM image of WO ₃ from plasma.	48
Figure 37.	Histogram of WO ₃ plasma Particle Size Distribution.	49
Figure 38.	XRD graph of combined WO ₃ commercial and plasma.	50
Figure 39.	XRD graph of WS ₂ produced from WO ₃ plasma.	51
Figure 40.	Combined XRD graph of WS ₂ with inset of WS ₂ commercial and WS ₂ plasma at 14° to show 2 theta shift.	53
Figure 41.	SEM image of WS ₂ from WO ₃ plasma.	53
Figure 42.	Histogram of WS ₂ plasma particle size distribution.	54
Figure 43.	TEM image of WS ₂ cluster.	55
Figure 44.	TEM image of WS ₂ plasma showing an isolated non-spherical WS ₂	55
Figure 45.	TEM image of WS ₂ plasma showing IF-WS ₂	56
Figure 46.	TEM image of WS ₂ plasma used for gap spacing measurements.	56
Figure 47.	Focused Ion Beam Milling was used to remove layer by layer to show the existence of hollow cores (indicated by arrows in some particles) as a consistent feature in the IF-WS ₂ sample produced from plasma WO ₃ precursor.	58
Figure 48.	XRD graphs of <i>in-situ</i> IF-WS ₂ and graphene from salts.	59
Figure 49.	XRD graphs of <i>in-situ</i> IF-WS ₂ and TEGO.	60
Figure 50.	SEM image of hybrid from WS ₂ plasma and TEGO.	61
Figure 51.	SEM image of hybrid from WS ₂ plasma and TEGO.	62
Figure 52.	XRD graphs of physical mixture hybrid.	62
Figure 53.	XRD graph of combined methods for producing hybrids.	63
Figure 54.	SEM image of physical mixture hybrid.	64
Figure 55.	SEM image of physical mixture hybrid to illustrate the IF-WS ₂ agglomerates and the placement of the IF-WS ₂ between the graphene sheets.	64
Figure 56.	Picture showing an epoxy composite compared to the neat epoxy mounts.	65
Figure 57.	Histogram of elastic modulus computed via nanoindentation.	67
Figure 58.	Histogram of normalized elastic modulus computed via nanoindentation.	68
Figure 59.	Histogram of hardness computed via nanoindentation.	69
Figure 60.	Histogram of normalized hardness computed via nanoindentation.	70
Figure 61.	Image showing the impact of a penetrator to a layer of fabric armor (from Stanford University's AHPARC, [online], Accessed 27 May, 2012).	71

Figure 62.	Illustration of shockwave impacting an IF-WS ₂ and the associated expected methods of deformation.	71
Figure 63.	Illustration showing the shock resistance testing for the scaled up material using military rounds.	74

THIS PAGE INTENTIONALLY LEFT BLANK

LIST OF TABLES

Table 1.	Settings used for XRD runs to determine composition of nanopowder materials.....	24
Table 2.	Parameters for nanoindentation.	29
Table 3.	Summary of XRD data for G,GO and TEGO.....	36
Table 4.	Summary of XRD data for WS ₂ from salts.....	40
Table 5.	Summary of XRD data for WO ₃ commercial.	41
Table 6.	XRD data for WS ₂ from WO ₃ commercial.....	43
Table 7.	XRD data for WO ₃ from plasma.....	47
Table 8.	XRD data for WS ₂ from WO ₃ plasma	51
Table 9.	XRD data for <i>in-situ</i> IF-WS ₂ and graphene from salts.	60
Table 10.	XRD data for <i>in-situ</i> IF-WS ₂ and TEGO.....	61
Table 11.	XRD data for physical mixture hybrid.....	63
Table 12.	Hybrid Composition by wt %.	65

THIS PAGE INTENTIONALLY LEFT BLANK

LIST OF ACRONYMS AND ABBREVIATIONS

$(\text{NH}_4)_2\text{WS}_4$	Ammonium Tetrathiotungstate
2D	Two Dimensional
Å	Angstroms
AC	Alternating Current
ACS	American Chemical Society
Cu	Copper
CVD	Chemical Vapor Deposition
EDS	Energy Dispersive Spectroscopy
FIB	Focused Ion Beam Milling
G	graphene
g	gram
Ga	Gallium
GO	Graphite Oxide
GPa	Giga-Pascal
H_2O	Water
H_2O_2	Hydrogen Peroxide
H_2S	Hydrogen Sulfide
H_2SO_4	Sulfuric Acid
H_3PO_4	Phosphoric Acid
HCl	Hydrogen Chloride
HRTEM	High Resolution Transmission Electron Microscopy
IED	Improvised Explosive Device
IF- WS_2	Inorganic Fullerene-Tungsten Disulfide
K	Thousand
keV	Kilo-electron Volts
kV	kilovolts
L	Liters
m	meters
mA	miliamps
mL	milliliter

mm	millimeter
N ₂	Nitrogen
nm	nanometer
psi	Pounds per Square Inch
PTFE	Poly-tetra Fluro-ethylene
rpm	Revolutions Per Minute
s	Seconds
SCCM	Standard Cubic Centimeters per Minute
SEM	Scanning Electron Microscopy
STEM	Scanning Transmission Electron Microscopy
TEGO	Thermally Exfoliated Graphite Oxide
TEM	Transmission Electron Microscopy
V	Volts
WO ₃	Tungsten Oxide
WS ₂	Tungsten Disulfide
XRD	X-ray Diffraction
μm	Micrometers

ACKNOWLEDGMENTS

First, I would like to thank my thesis advisor, Professor Claudia Luhrs, who has been an inspiration both personally and professionally, whose guidance inspires me to believe in the future of science and my ability to play an active role in shaping that future.

From our research group, I would like to specifically thank ENS Michael Moberg, LT Ryan Palinuik, LT Jamie Cook, LCDR Chris Daskam, LT Jason Downs and LT Russ Canty for their teamwork and the many hours in the lab together to create a better future for our soldiers and sailors.

I would like to thank Professor Sarath Menon and Professor Luke Brewer for the patience and understanding when it came to instructing me in the use of the materials characterization equipment. Their guidance is greatly appreciated.

Also at NPS I would like to thank Katy Love for all her behind-the-scenes work, which helped keep me sane by showing me the right way to complete any paperwork and the most efficient way to get things accomplished in our department.

Last, I would like to thank my husband, Ryle Maxson, for his quiet understanding and desire to help whenever possible. He is the person who constantly believes in me and my ability to achieve whatever I can dream.

THIS PAGE INTENTIONALLY LEFT BLANK

I. INTRODUCTION

A. Overview

This manuscript presents some of the ongoing efforts at the Naval Postgraduate School to develop new lightweight materials for personal protection applications. Hybrid nanostructures combining carbon based architectures (Graphene) and ceramic particles (Inorganic Fullerene type WS_2) are the central focus of the study, along with their epoxy-based composites.

Current armor systems employ diverse strategies to stop a penetrator and absorb or attempt to disperse its impact energy. Multiple research groups have been aiming to develop new ballistic resistant materials, from ballistic fibers to combinations of those with other strong organic and inorganic (ceramic, metal) material layers. However, even with the novel materials that might allow a penetrator to be stopped and an open wound prevented, the dissipating energy from an impact could still cause non penetrating injuries, known as blunt force trauma. Moreover, the most effective systems we currently employ contain materials that will add considerable weight to the wearer—a situation that poses the challenge to develop materials that could reduce the possibility of blunt force trauma while reducing the weight of the overall component.

B. Advances in Personal Protection Systems

Current personal protection body armor in use is a vast improvement over the animal hides and chain mail our descendants wore many years ago [1]. Today's body armor contains a plate comprised of ceramic or metal combined with some fabric designed to stop not only bullets but shrapnel and other materials fragments that could result from an improvised explosive device (IED). High performance fibers used in personal protection should have low density, high strength and high energy absorption capabilities. Glass, aramid (Kevlar, Twaron), and high performance polyethylene (Dyneema, Spectra) fibers have been already introduced into the market to fulfill the need for materials with such properties. The most well-known of the personal protection fabrics is Kevlar, first created in the 1970s by Dupont, which is both ballistic and stab-

resistant [2]. Regarding the ceramic and metal plates, clay and boron nitride are the most common in the former category, while steel, titanium and aluminum for the later.

The lighter weight option (seen in Figure 1) that could be used in the field is to wear only fabric materials such as the one listed above; essentially, the user wears many layers of the fabric compressed into a vest and foregoes the heavier option of the ceramic or metal plates. This dramatically reduces the weight of the material being worn, but lowers the level of threats the body armor will be able to withstand. Often such operating environments force soldiers to choose between wearing body armor that fully protects them, or a lighter weight body armor. The first option might cause them to underperform, or in the most extreme cases, lose consciousness while wearing the armor, since they can already be carrying up to 70 pounds of gear, while the second option will increase their vulnerability. Furthermore, the body armor, even without the ceramic or metal plates, is very restrictive, often not allowing the wearer a full range of motion which poses a whole new level of threats simply by altering the way the wearer moves and functions while wearing the body armor.



Figure 1. Photograph of two sailors wearing a “light” version of body armor (Image used with permission from LT Melanie Chambers and LT Kathryn Johnson).

The research for new body armor technology is focused primarily on addressing the functionality of the material, reducing the weight levels and increasing wearer flexibility. Through our research, we aim to use nanomaterials to develop architectures with increased level of protection for our soldiers and sailors while at the same time reducing the weight of the systems.

Nanomaterials have emerged in last decade as an alternative to improve mechanical properties of polymeric composites, in particular, carbon nanotubes have been extensively studied in diverse systems at various loadings [3–8]. Tungsten disulfide nanoparticulates have been extensively used as lubricants and only in recent years, with the development of inorganic fullerene type structures of WS_2 (IF- WS_2), have these materials attracted attention as filler in composites for armor applications. Only a few attempts have been made to combine either carbon nanofibers or other graphitic structures with WS_2 spherical particles [9–12]. No published references exist to date with regards to hybrids combining graphene and IF- WS_2 .

C. Graphene as Component

Graphene is the name given to a sheet composed from one to a few atomic layers of hexagonally bonded carbon atoms. The structure can be described as an infinite two dimensional molecule, as the one depicted in Figure 2. The graphite structure is composed by a large number of graphene layers kept together by van der Waals interactions.

Graphene is impressively lightweight, it has a theoretical surface to weight ratio of 2, 700 m^2/g and it is incredibly strong with a calculated tensile strength of ~ 130 GPa [13]. The potential applications proposed for graphene arise from several unique features: the mechanical strength inherent in the strong covalent bond between adjoining carbon atoms in a basal plane, the ability of graphene to be organized into circuit elements at molecular scale and the particular chemistry of the edges of its sheets.

Those properties lend itself to the graphene inclusion in lightweight architectures, especially considering the 2D structure of graphene, where 3,000,000 sheets are ~ 1 mm thick, which means the thickness of the material can be kept to a minimum. Graphene is a

low cost material that can be produced by multiple methods with diverse degrees of exfoliation and surface functionalities, which is not a critical factor for its use in basic research projects, but certainly an added value for using the material in a large-scale implementation of the design.

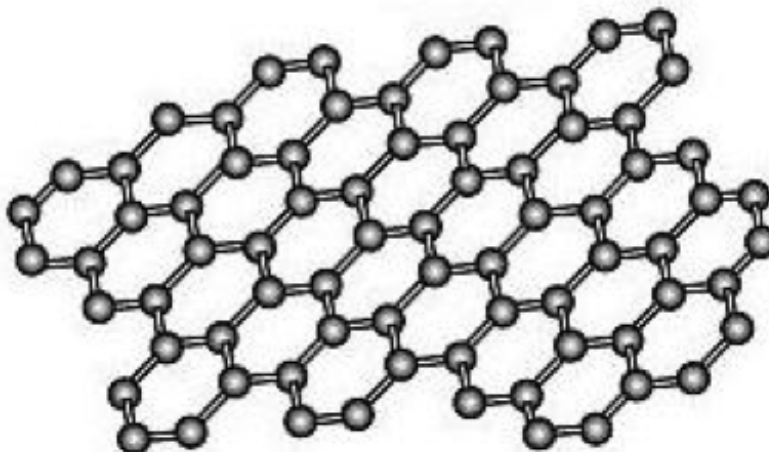


Figure 2. Graphic representing the 2D structure of graphene [13].

D. Tungsten Disulfide Structures

The most common microstructure found in WS_2 consists of expanded layers, similar to the ones encountered in graphite. Although, it is the closed cage structure, which particles are usually on the nanometer scale, which are the focus in this manuscript.

Carbon was once believed to be the only material able to create nanowires and closed geometric shapes such as carbon nanotubes and fullerenes. The closed-cage type polyhedral structures, however, are no longer limited to carbon; the discovery of similar inorganic forms made from other components, such as WS_2 and MoS_2 is opening up vast new opportunities. These new material nanostructures provide a larger variety of material properties, which allow for many more applications. Over time, research has shifted a good portion of its focus from organic to inorganic structures. Some of the reasons for this shift are as follows: inorganic fullerenes have been broadly tested and are considered

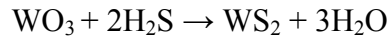
safe compared to the toxic organic fullerenes; they are more stable and less reactive than the organic fullerenes, and organic fullerenes have a more expensive and toxic growth process.

Chemical bonds are not stable beyond the distance of a few angstroms; as a result, general chemistry does not favor materials with empty space. Atoms within materials arrange themselves in close proximity to their nearest neighbors in order to maximize the interaction between electron clouds and stabilize the chemical bonds between them. Consequently, the scientific investigation of hollow-closed structures was almost wholly unexplored until the latter part of the 20th century. The first serious inquiries were undertaken by Linus Pauling in 1930, where he investigated closed polyhedral and tubular forms of asbestos minerals such as kaolinite (alumino-silicate) [14]. However, the turning point in the scientific exploration of hollow closed atomic structures occurred with the discovery of carbon fullerenes by Kroto, Smalley, and Curl in 1985 and later with carbon nanotubes by Iijima in 1991 [15, 16]. The first inorganic fullerene-like nanoparticles of WS_2 were discovered by Tenne and his colleagues working at the Weizmann Institute of Science in 1992 [17]. Via a method of diffusion-controlled sulfurization of metal oxides, they were able to empirically prove the existence of such phases of inorganic compounds. Shortly thereafter, the discovery of inorganic nanotubes and fullerene-like structures led to the establishment of a new field of inorganic chemistry; one dealing with the polyhedral or closed-hollow nanostructures of materials [18]. A few of the applications recently proposed for such structures include processes such as filtering, shielding, lubrication, composites filling, and sensors [19–21].

WS_2 has been found in morphologies such as nanospheres, nanotubes, nanoflowers, nanoribbons, nanoropes, nanoflasks and nanocones [10, 19, 22–29]. Depending on the formation scheme and experimental conditions, though under the same chemical reaction, these various forms can be obtained.

The term “Inorganic Fullerene-like” (IF) was coined for the resemblance between IF- WS_2 to carbon based nested fullerenes, both in properties and in appearance. IFs are primarily the spherical layered structures seen in Figure 3. Each layer is weakly bonded

to the next by Van der Waals forces and so can be easily exfoliated when damaged without altering the inner layers. This property has led many to investigate the tribology of these particles which will be discussed later. After many years of research, it was determined that for sulfides generated from tungsten oxides both outside-in and inside-out formation schemes occur. For the more reported outside-in method, the “partially reduced core is converted into metal-sulfide in a quasi-epitaxial layer by layer process, leading to a nested multilayer core” [18]. If the reaction proceeds to completion, the IFs have a hollow core. The reason for the hollow core is seen in the chemistry,



where one sulfur atom replaces one and a half oxygen atoms [21]. In the inside-out formation method, the reactants are vaporized and initial nuclei are formed. Eventually these structures grow and at a critical size they bend and form IF structures which continue to grow and crystallize. When the clusters are smaller than this critical size, many point defects and dislocations are found, often resulting in partially closed polyhedra [30].

The decision to use tungsten disulfide (WS_2), specifically IF- WS_2 , was based on its properties as a lubricant and its ability to withstand very high shock pressures. Recent research has found that IF- WS_2 is able to withstand shock pressures of 25 GPa, which would be necessary for our application within the matrix of the body armor. It was found that in MoS_2 with particle size of 80 nm and same inorganic fullerene shape was able to withstand shock pressures in excess of 130 GPa [30].

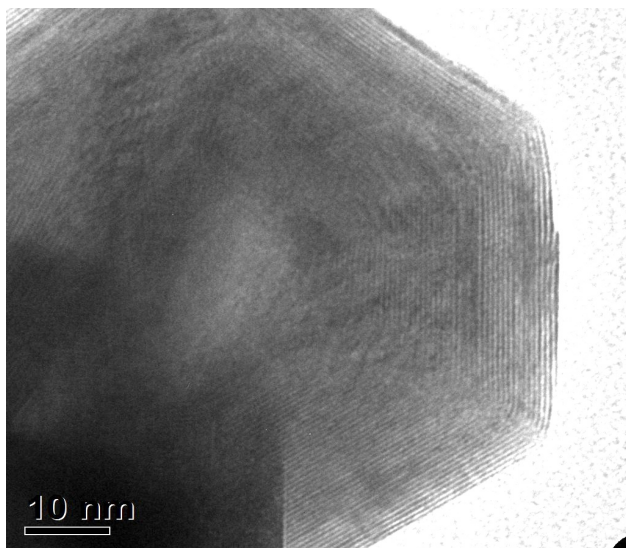


Figure 3. Transmission Electron Microscope image of IF-WS₂ showing the inorganic fullerene structure the brighter core is evidence of a hollow interior.

E. Thesis Objectives

The general scope of this thesis is centered on the development of nanometric architectures which individual components interaction and light weight could render improved impact or shock resistance composites for potential use in personal protection systems. In particular, we aimed to design a nanohybrid that combined the potential of graphene sheets with the characteristics of IF-WS₂.

Moreover, both graphene and IF-WS₂ nanostructures have been prepared by diverse routes, but no attempts have been made to design the structures to optimize the morphology for impact or shock absorbing properties. For graphene, more than individual sheets, agglomerated or crumpled sheets will present the empty spaces and flexibility of typical energy absorbing structures. For IF-WS₂ a small particle size and large angles in the polyhedra are sought, since those characteristics could, according to literature in the field, enhance the mechanical properties. No other groups have attempted to combine these individual materials before and new protocols to integrate them are needed.

The thesis is divided into five chapters that present in a systematic way how the materials were prepared and integrated as hybrids first and epoxy composites later along

with the fundamentals of the methods and techniques used to characterize their crystal structure, microstructure and mechanical properties. All the results are presented in a chapter that also discusses the above. The manuscript then summarizes the milestones achieved and compares the data with the ones previously found in a similar system, CNF/IF-WS₂. Suggested next steps to further the research are also included.

F. Hypothesis

The use of graphene and IF-WS₂ hybrid nanomaterial will improve the mechanical properties of composites in which the hybrid will be included, in particular, epoxy based systems. The light-weight of the new Graphene/IF-WS₂ composites could allow current personal protection systems to increase user protection, while the protection system weight is maintained or reduced.

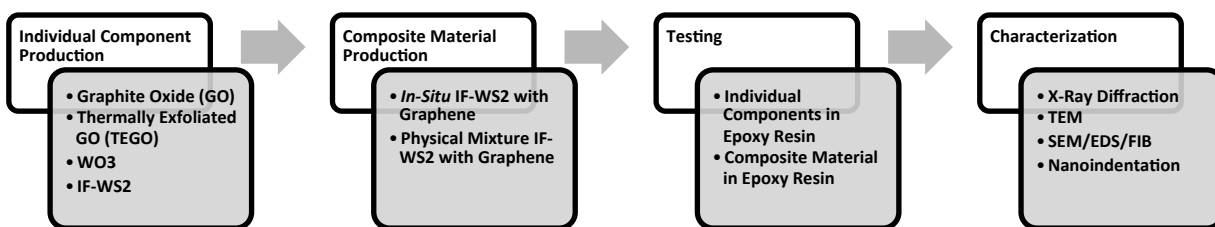
G. Naval Relevance of the Topic

A positive outcome of this research will provide better understanding of which nano-structure characteristics could help dissipate the energy of an impact or the associated shock wave. The improvement of the material properties used in body armor will add to the level of protection, flexibility and desire for wearing the vest by the soldiers and sailors in the operating environments.

II. EXPERIMENTAL METHODS

A variety of equipment and techniques to create both individual nanopowder components and the hybrid composite consisting of the IF-WS₂ and graphene were employed. This chapter will summarize the steps followed for the fabrication protocols, the operational principles for the techniques and conditions of analysis.

A diagram (see below) will be used to guide the reader through the different materials that were synthesized throughout the manuscript. As a new topic or synthesis is covered, the diagram will highlight it to provide emphasis and reference for where that step lies within the overall research. For the subheadings (i.e., graphite oxide production), the diagram is abbreviated to emphasize the material covered, expanding to the large diagram when a new heading (i.e., Composite Material Production) will be discussed.



A. Synthesis Of Individual Component Nanoparticles

In order to integrate graphene and IF-WS₂, precursors for the same had to be generated; for graphene, graphite oxide (GO) and for IF-WS₂, WO₃. This section will describe the synthesis of both.

1. Graphite Oxide Production

This section covers the production methods used to synthesize graphite oxide, using both graphite flakes and nanopowder, thermally exfoliated graphite oxide and inorganic-fullerene tungsten disulfide. For the production of GO we used both graphite flakes and graphite nanopowder. Graphite oxide was produced based on a further modification to the method reported by Marcano *et al*[8].

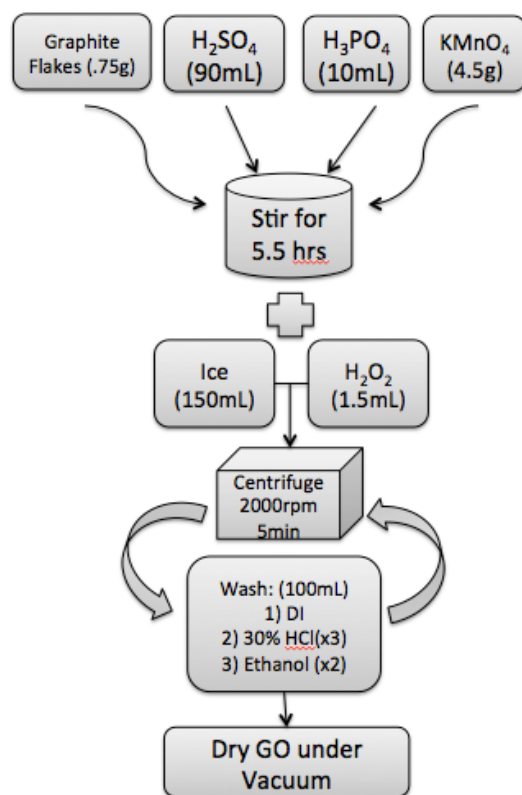


Figure 4. Stepwise production of Graphite Oxide.

The synthesis (see Figure 4) used a 9:1 mixture of 90 mL H_2SO_4 (Sigma-Aldrich ACS reagent 95.0–98.0%, catalog number 258105–500ML) to 10 mL H_3PO_4 (Sigma-Aldrich ACS reagent, ≥ 85 wt. % in H_2O , catalog number 438081–500ML). To this we added graphite flakes (Aldrich Graphite Flakes, particle size +100 mesh, $\geq 75\%$ min, catalog number 332461–2.5KG) in the amount of 0.75 g, or graphite nanopowder (Aldrich Graphite Powder, $< 20 \mu\text{m}$, synthetic, catalog number 282863–25G) for reasons that will be described in detail later. Following the addition of the graphite nanopowder the mixture was sonicated for one minute until the mixture was homogenous. Using a Bransonic Ultrasonic Model 2510R-MTH Sonicator (see Figure 5, Left) operated at room temperature.

The mixture was then placed on a Corning hotplate and stirrer (AC input 120 V, 4"x5") , used in conjunction with a Spinbar[®] magnetic stir bar at 240 rpm (PTFE-coated octagonal, size 1"x3/8") to ensure mixtures in solution remained as a homogeneous dispersion (see Figure 5, Middle).

Then 4.5 g of KMnO_4 (Mallinckrodt Baker Inc., ACS Reagent, 3227–01, 500 g) were added, at which point a slight exothermic reaction was observed, which increased the temperature to 35°C.

This mixture was allowed to continue stirring under the vent hood for five and a half hours, at which point ice cubes made from 150 mL of distilled water were added to the mixture. Once the ice cubes were completely dissolved, 1.5 mL of H_2O_2 (Sigma-Aldrich Hydrogen peroxide solution, contains inhibitor, 30 wt. % in H_2O , ACS reagent, catalog number 216763–500ML) were added drop wise. At this point in the oxidation process, bubbles were formed and a more exothermic reaction was observed, with the temperature increasing to 45°C or 55°C for the graphite flakes and graphite nanopowder respectively. The mixture was stirred for another hour and then allowed to settle overnight (see Figure 6, Left).

The particulates settled to the bottom of the beaker, and the excess liquid was removed via pipetting. The remaining material was divided between two 50 mL centrifuge tubes. The mixture was then centrifuged for five minutes at 2000 rpm, in a Hermle Z300 Centrifuge (see Figure 5, Right) fitted with a 4 x 50 mL rotor.

After being centrifuged the excess liquid was drained from the top and replaced with 20 mL of deionized water. The centrifuge tube is shaken until no mixture remains adhered to the sides. The tubes were replaced in the centrifuge and again set at 2000 rpm for five minutes. The excess liquid was drained and replaced with 20 mL of 30% HCl solution (prepared from Sigma-Aldrich Hydrochloric acid ACS reagent, 37%, catalog number 320331–500ML) and shaken before being centrifuged. The use of the 30% HCl solution was repeated three more times (or until the excess liquid did not have remnant MnO_2 evident by a transparent solution). The final washing step was performed twice with 20 mL of ethanol (Sigma-Aldrich, ACS Reagent, $\geq 99.5\%$, 200 proof, absolute, catalog number 459844–500ML), and the excess liquid drained. The mixture was poured into a small dish (see Figure 6, Middle) for drying in a Nalgene vacuum desiccator (with stopcock, overall H 262 mm) using a pump to achieve vacuum, which was used to dry the resultant graphite oxide (see Figure 6, Right).



Figure 5. Left) Bransonic Ultrasonic Sonicator Middle) Corning Hotplate and Stirrer Right) Hermle Z300 Centrifuge with 4x50 mL Rotor.



Figure 6. Left) Mixture of Graphite Powder with Acids and KMnO_4 and H_2O_2 at the end of the Reaction Time Middle) GO prior to being placed under vacuum Right) Nalgene Vacuum Desiccator with Graphite Oxide Drying.

2. Thermally Exfoliated Graphite Oxide (TEGO) Production

After being placed under vacuum, the GO was thoroughly dried and ready for exfoliation. For each run 0.05 g of GO were measured and hand crushed in a mortar and pestle for fifteen minutes, the material was then spread evenly along the bottom of an alumina boat (Sigma-Aldrich, Coors combustion boat, high-alumina, 70 L x 14 W x 10 mm H, 5 mL capacity, catalog number Z561738–1EA). The boat was sealed inside the Thermo Scientific Lindberg Blue M 1200C tubular furnace (see Figure 7, Left).

This furnace has a single point temperature control and a heated length of twelve inches; for synthesis a one-inch diameter quartz tube was used with a ceramic boat inserted and sealed up with high-temperature O-rings inside of stainless steel fittings. An inert nitrogen atmosphere was used for the exfoliation, which flow was regulated using a MKS multi-gas controller 647C (4 channels) with an initial pressure of 20 psi supplied from the gas cylinder, or supplied via a Matheson flow meter (E100) (see Figures 7, Middle and Right).

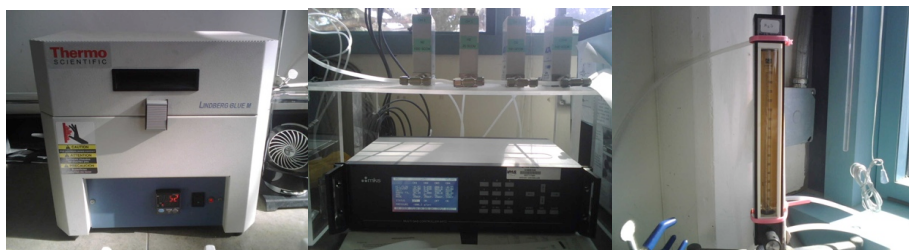


Figure 7. Left) Thermo Scientific Lindberg Blue M Tubular Furnace Middle) mks Multi Gas Controller 647C. Right) Mattheson E100 Flowmeter for Hydrogen Sulfide.

The furnace was heated to 800°C and the flow of the N₂ dropped to 15 SCCM. Once 800°C was achieved, the material was left at this temperature for fifteen minutes. The TEGO is cooled to room temperature and then collected. The yield of the synthesis was typically 0.02 g of TEGO was collected (some material was lost during collection).

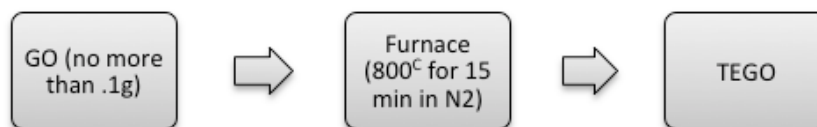


Figure 8. Stepwise production of TEGO from GO.

3. Inorganic Fullerene Type WS₂ Production

Three different methods for producing the IF-WS₂ were attempted, one used commercial WO₃ and the other two used ammonium tetrathiotungstate (NH₄)₂WS₄ as a precursor and will be discussed in detail below.

a. From Ammonium Tetrathiotungstate Salts

Ammonium Tetrathiotungstate decomposes upon heating to generate WS₂ as a single solid byproduct. It has been previously used by Chen *et al.* to provide WS₂ fibers [22].

For this synthesis 0.13 g of (NH₄)₂WS₄ was measured and then crushed by hand in a mortar and pestle for fifteen minutes. The material was then evenly dispersed into the bottom of an alumina boat and sealed inside the quartz tube of the furnace. The

atmosphere was purged with N₂ at 200 SCCM for twenty minutes, at which point the furnace was turned on and heated to 600°C. The material remained at 600°C for two hours in the same atmosphere of N₂. After two hours the furnace was shut off, and the material allowed to cool to room temperature, with the N₂ left flowing the entire time. Upon reaching room temperature, the N₂ flow was shut off and 0.084 g of WS₂ was collected.



Figure 9. Stepwise production of WS₂ from (NH₄)₂WS₄.

b. From Plasma Generated Tungsten Oxide

Using the plasma torch (see Figure 10), the precursor of (NH₄)₂WS₄ was finely crushed and carried through the plasma region of the plasma torch at atmospheric conditions using Argon gas. As the precursor was carried into the discharge region the material was subjected to temperatures in excess of 3500°C for very small amounts of time, less than a second. The material was altered in the plasma discharge region and the spherical particulate shape was achieved in the chimney where rapid cooling takes place, and the new particulates were captured on the filter after the cooling [31].



Figure 10. Aslex Atmospheric Microwave Plasma System used to create WO₃.

An Aslex Atmospheric Microwave Plasma System operating at 900 Watts, 2455 MHz frequency was used for the production of spherical WO₃. The ammonium tetrathiotungstate was used as a precursor and Argon as plasma gas. Argon/air mixtures were employed as carrier gas.

To sulfurize the product, the WO₃ from plasma, 0.067 g was evenly dispersed in the bottom of an alumina boat and then placed inside the quartz tube and sealed up inside the furnace. The sample was purged in N₂ for twenty minutes at 200 SCCM before being heated to 900°C. Once the temperature reached 900°C, the N₂ flow rate was reduced to 100 SCCM and H₂S was added in at 3.98 SCCM. The flows remained unchanged for three hours, while the temperature was stable at 900°C. After three hours the H₂S gas flow was discontinued. The material was allowed to cool to room temperature in the N₂ atmosphere. Once cooled, the N₂ flow was turned off and 0.069 g of WS₂ were collected.

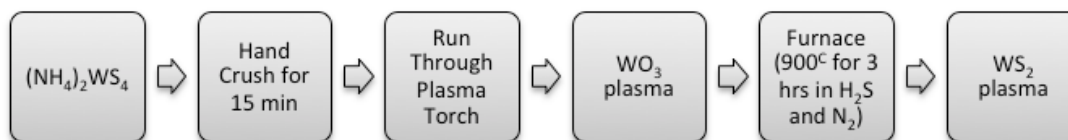


Figure 11. Stepwise procedure for producing Plasma IF-WS₂ from (NH₄)₂WS₄.

c. *From Commercial Tungsten Oxide Particles*

Commercial Tungsten (IV) Oxide, 0.67 g (Sigma-Aldrich, ~20 μm, catalog number 232785–100G), was hand crushed in a mortar and pestle for fifteen minutes and then evenly dispersed in the bottom of an alumina boat. An identical procedure to the one described in section 3b above was followed to sulfurize the particles,

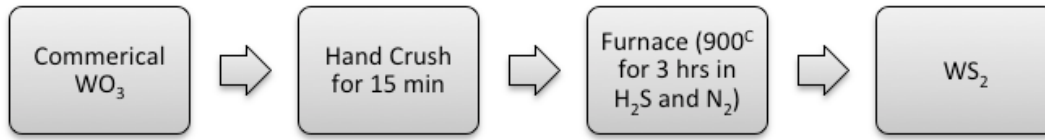
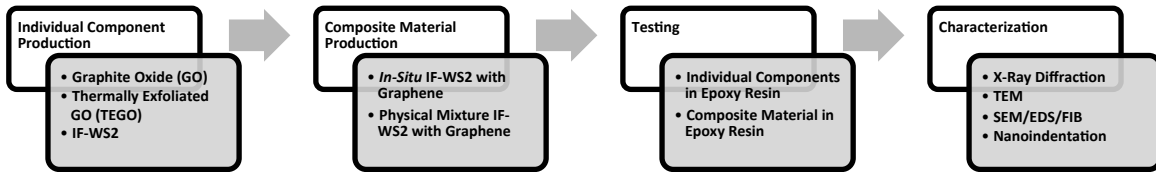


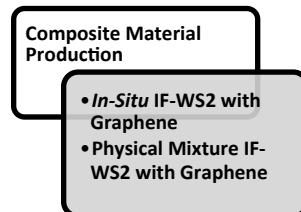
Figure 12. Stepwise procedure for production of WS₂ from commercial WO₃.

B. Fabrication of Hybrid Composite Graphene/IF-WS₂

For the creation of the hybrid materials, to keep the weight at a low level, the inclusion of the IF-WS₂ will be kept to around 1%. Since the graphene sheets weigh much less, the inclusion of 1% should be a minor addition in weight, and will also allow for comparison of results to ENS Michael Moberg's thesis work.



Two different methods were used to create the hybrid composites, a material comprised of 99% thermally exfoliated graphite oxide and 1% inorganic fullerene-tungsten disulfide. The first method was to create the hybrid composite *in-situ*, while the second method was to create the individual components, as described above, and combine the components physically to create the hybrid composite.



1. *In-Situ* Production of Graphene/IF-WS₂

The integration of graphene with IF-WS₂ could be performed in a number of various ways. The first method employed consisted of taking 0.15 g of the commercial WO₃, 0.3 g of the GO and 1.6 g of urea; it was hand crushed together for fifteen minutes before depositing evenly on the bottom of an alumina boat. The boat was placed inside the quartz tube within the furnace and purged with N₂ for twenty minutes at 509.78 SCCM. After the twenty-minute purge, the furnace was heated to 600°C and the material left at that temperature for fifteen minutes. The non-sulfurized sample, comprised by graphene and WO₃, then cooled back to room temperature and 0.25 g of sample were collected for analysis.

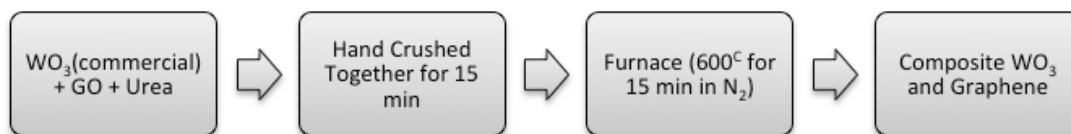


Figure 13. Stepwise procedure for in-situ non-sulfurized composite.

An alternate variant used for fabrication of the hybrid graphene/IF-WS₂ involved the use of 0.10 g of (NH₄)₂WS₄ with 0.11 g of GO and 0.57 g of urea which were hand crushed together in a mortar and pestle for fifteen minutes before being distributed along the bottom of an alumina boat. The sample was placed in the furnace and purged with N₂ for twenty minutes at 330.17 SCCM; after the purge was completed the furnace was heated to 600°C. Once the furnace was stable at 600°C, the material was heated for fifteen minutes, after which the furnace was shut off and the material cooled to room temperature. Once the material reached room temperature it was collected for analysis.



Figure 14. Stepwise procedure for first in-situ sulfurized composite.

In the initial stages for hybrid generation ammonium tetrathiotungstate salt with urea were used, although the final product contained irregular shape particulates and large size distribution of the same. Given that result, the production of IF-WS₂ was limited to the use of WO₃ as a precursor. The urea was initially added to aid the exfoliation of the GO powder, although in later steps its use was discontinued in favor of a combined exfoliation and sulfurization process. Graphene exfoliation and removal of oxygen groups in the structure are more efficient when they occur at higher temperatures, so subsequent exfoliations occurred at 800°C without the inclusion of urea.

After refining the protocol, the primary method utilized to produce the graphene/IF-WS₂ hybrid, that will be now referred to as *in-situ*, consisted of mixing 0.0059 g of WO₃ plasma and 0.7996 g GO. The components were combined and ground with mortar and pestle for fifteen minutes, placed in an alumina boat and inserted in the furnace. The sample was purged in N₂ at 330.17 SCCM for twenty minutes and then heated to 800°C for exfoliation. Once the furnace was stable at 800°C the sample was exfoliated for ten minutes. The sample was then allowed to cool to room temperature and collected 0.1731 g of non-sulfurized composite.

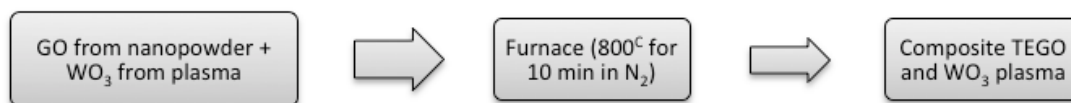


Figure 15. Stepwise procedure for non-sulfurized composite from plasma WO₃.

The sample was purged in 330.17 SCCM N₂ for twenty minutes, after which time the furnace was set to heat to 900°C. At the same time, the N₂ flow was reduced to 150.52 SCCM and H₂S was added to the flow at 3.9839 SCCM. Once the furnace temperature reached 900°C the material was left to sulfurize for three hours. After three hours the furnace was turned off and the flow from the H₂S was stopped. The N₂ flow was set to 150.52 SCCM until the sample reached room temperature, after which the flow was halted. The sample was then collected, and 0.0263 g of sulfurized hybrid were obtained.

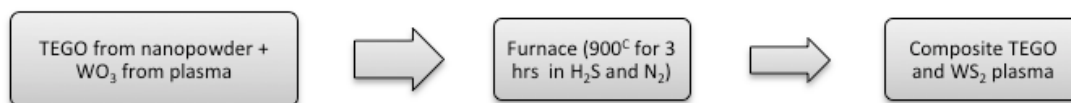


Figure 16. Stepwise procedure for sulfurized composite from WO_3 plasma.

This above method was further modified, the sample was kept in the furnace after initial exfoliation in N_2 and then heated to 900°C in H_2S atmosphere to sulfurize the tungsten oxide by using the remaining non-sulfurized composite, 0.0421 g, and placed in an alumina boat inside the furnace. The material was then purged with N_2 at 200 SCCM for twenty minutes, after which it was heated to 900°C for three hours. When the heating was started, the flow for the N_2 was reduced to 100 SCCM, while H_2S was added at 3.9839 SCCM. After three hours the furnace and H_2S were shut off, and the material was allowed to cool to room temperature. There was 0.0235 g of sulfurized composite material collected.

2. Physical Mixture of WS_2 with Graphene

This method combined 0.0009 g of sulfurized WO_3 plasma (now IF- WS_2 plasma) and 0.009 g TEGO (from nanopowder) in a sample vial. The vial was then sonicated for five minutes at room temperature and then stored.



Figure 17. Stepwise procedure for physical mixture of sulfurized composite.

C. Generation of Epoxy Resin Composites

Epoxy resin mounts were used to suspend the nanomaterials in order to measure the hardness and Young's Modulus of the materials against a baseline established by a mount created solely of epoxy. For this purpose, Struers Specif-Fix 20 Kit (see Figure 18) was used.



Figure 18. Struers Specifix 20 Kit used to create epoxy mounts.

The epoxy mount was created using the two separate solutions, one being the resin and the other the hardening agent. By volume, it was required to use a ratio of 5.1:1 of the resin to the hardening agent. Once the two solutions were combined, there were 60 minutes during which the material would remain pliable and allow the addition of the nanomaterials. The epoxy molds held approximately 27 mL of the epoxy, and for the samples, 1% loading of the epoxy was desired, which meant that often a smaller amount of epoxy was created and then backed with the pure epoxy mixture.

To create the epoxy mount, a sterile plastic cup was used to hold the material, and the required amount of resin was measured and poured into the plastic cup. To this the 1% of nanomaterials was added and stirred vigorously for two minutes, after which it was sonicated for three minutes to create a homogenous mixture. To this mixture, the required amount of hardening agent was added and then stirred vigorously for a period of two minutes, after which the mixture was sonicated for another three minutes until the mixture was homogenous. After the sonication, the solution was poured into the 1 ¼” silicone mold (see Figure 19, Top).

For several mounts it was necessary to let them cure for 24 hours before creating a ‘neat’ solution, comprised solely of resin and hardening agent, which was poured into the mold to act as a backing for the epoxy with nanomaterials. The epoxy molds were covered for a week to facilitate a complete curing of the material. After one week passed, the mounts were removed from the mold.

After 30 days, the mounts were prepared for nanoindentation (see Figure 19, Middle), whereby it was necessary to finish the surface of the epoxy mount, as a highly polished surface was desired to get accurate results from nanoindentation. The first step for polishing involved grinding down the surface on different grit sandpapers. The sandpaper was wetted, and then the puck was ground in the following order: 240-grit, 320-grit, 400-grit and lastly 600-grit sandpaper. When the results of the grinding were satisfactory, the mounts were then polished using polishing wheels fitted with polishing media at 1 μm and 0.05 μm respectively. Once a highly polished finish was achieved, the epoxy mounts were ready to proceed to nanoindentation (see Figure 19, Bottom).

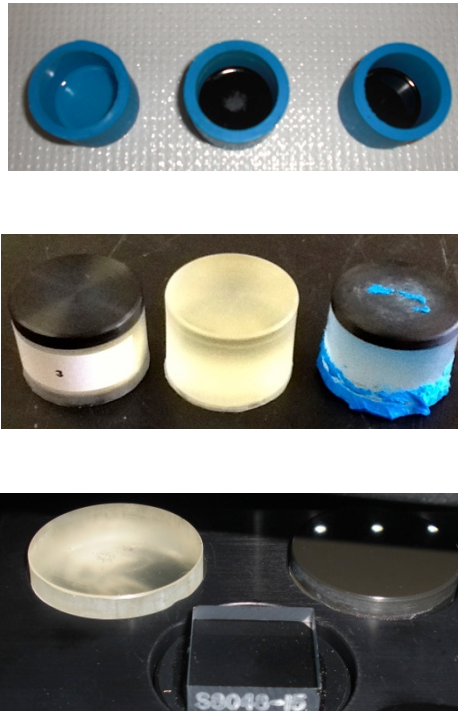
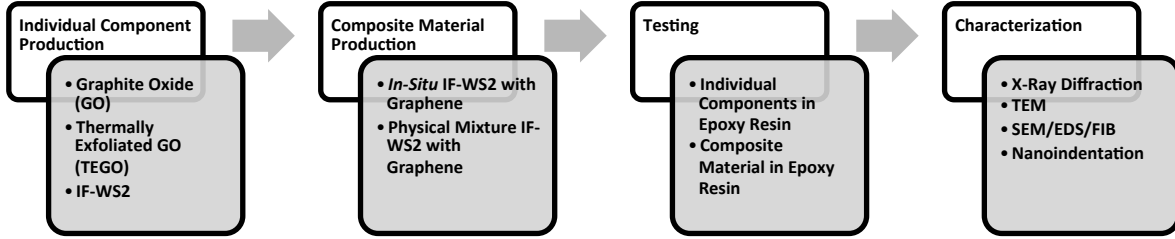


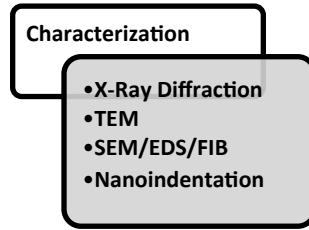
Figure 19. Top) Silicone molds with 1% nanomaterials loading in the epoxy Middle) Epoxy mounts removed from the molds (center being neat and outer two with 1% loading). Bottom) Highly polished surface of epoxy mounts in tray of nanoindenter.

THIS PAGE INTENTIONALLY LEFT BLANK

III. CHARACTERIZATION



Once the material, individual or composite, was synthesized, it was ready for analysis to determine the composition, crystalline structure, morphology, particle size, as well as identify any impurities that were present. Various techniques were used to achieve this end, specifically X-ray diffraction (XRD), transmission electron microscopy (TEM), scanning electron microscopy (SEM), energy-dispersive X-ray spectroscopy (EDS), focused ion-beam milling (FIB), and nanoindentation.



A. X-Ray Diffraction

The materials synthesized, both individual and composite, consisted of solid powders and were crystalline in nature, and provide the ideal platform to be analyzed by X-ray diffraction.

The software suite then analyzed the reflected X-rays to provide the data in a set of counts that was represented in graphical form, which revealed the various d-spacings that are unique to the individual nanopowder being analyzed. These d-spacings were compared to the database of the International Centre for Diffraction Data. The patterns that match were given a percentage ranking, which provided the operator the ability to select only patterns that indicated a match based on the counts and d-spacing.

The X-ray diffractometer used is a Phillips Type PW1830/40 Analytical X-ray B.V. with a PW1830 generator. The samples were placed on a zero-background slide, made from a silicon crystal and inserted in the sample holder for analysis. The software was programmed with the following parameters for each XRD run:

Start Position [$^{\circ}2\theta$]	5.000
End Position [$^{\circ}2\theta$]	70.000
Step Size [$^{\circ}2\theta$]	0.0200
Scan Step Time [s]	2.0000
Scan Type	Continuous
Offset [$^{\circ}2\theta$]	0.0000
Anode Material	Cu
K-Alpha1 [\AA]	1.54060
K-Alpha2 [\AA]	1.54443
K-Beta [\AA]	1.39225
K-A1/K-A2 Ratio	0.50000
Generator Settings	10 mA, 10 kV

Table 1. Settings used for XRD runs to determine composition of nanopowder materials.

Once the settings were established, the XRD was powered on and the settings gradually increased till 30 kV and 35 mA were reached. After this was achieved, the software suite ran the selected program (see parameters in Table 1), which took one hour and 18 minutes to complete.

All the reflections shown in the XRD patterns correspond to pure phases, except when stated otherwise in the XRD figures.



Figure 20. Image of X-ray diffractometer.

B. Transmission Electron Microscopy

The TEM operates similar to an optical microscope; however, a beam of electrons is used instead of a light source to obtain images of the material being examined. The nanopowders were suspended in ethanol and then deposited on a mesh slide to obtain the very thin layers required when using a TEM. In Transmission Electron Microscopy, the electron beam was provided by an electron source, which was directed to the material being analyzed. The electrons then pass through the specimen, after which they were filtered by a series of electromagnetic lenses and finally displayed on a viewing screen. Because the specimen had been prepared to have little density on the mesh of the slide, this allowed the electrons to give an image indicative of the structure of the material, including all the nuances of the material, such as the inorganic-fullerene type rings that should be visible in the WS₂ samples.

The TEM data was collected at the University of New Mexico with a JEOL 2010 high resolution transmission electron microscope (HTEM) and JEOL 2010F FASTEM field emission gun scanning transmission electron microscope (STEM/TEM) equipped with Gatan GIF image filtering system. Samples were prepared by dispersing the powders in a few mL of ethanol and a drop of the dispersion was placed in a copper holey-carbon TEM grid where the ethanol was allowed to evaporate prior to the sample being viewed.

C. Scanning Electron Microscopy

The SEM also uses electrons, instead of a light-source, to project an image of the surface of the sample. The electron gun provided a beam of electrons, which passed through an anode, magnetic lens and coils to focus the beam. The specimen was loaded onto a stage and placed inside a vacuum chamber, where the sample would be scanned by the electron beam, allowing for the surface of the material to be viewed using the in-lens detector. Through manipulation of the stigmation and alignment, an image of the surface was achieved; at lower magnifications a broad picture of the surface was obtained, useful for particle size determination. At higher magnifications, it was possible to discern differentiations in individual particles, as well as focus on the dispersion patterns.

SEM images were collected using a Zeiss Neon 40 Crossbeam Scanning Electron Microscope with a Schottky type field emission system. The system was set to 20 kV and 0.33×10^{-6} mA. Images were collected at 2K, 4K, 8K, 16K, 32K, 40K, 60K, and 90K magnifications to get both a broad and close-in feel for the structure of the samples. Images were collected with the software and stored in jpeg format.

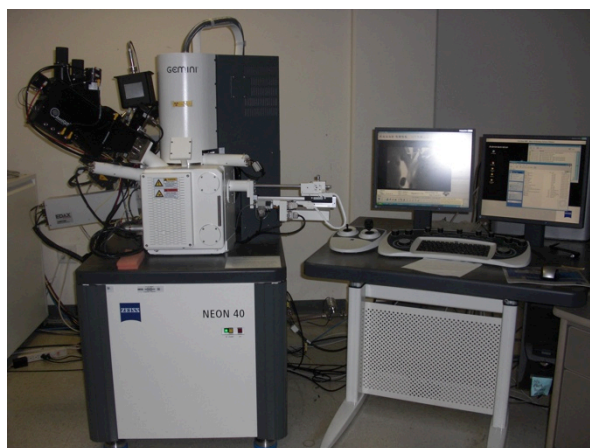


Figure 21. An image of the Zeiss SEM used to capture surface images of the samples.

Furthermore, the SEM images were used to obtain particle size distributions. The image was evaluated using open-source software, ImageJ, to manually measure each particle's diameter in diverse pictures representative of each sample to generate a histogram of the number of particles vs. size distribution.

D. Energy-Dispersive Spectroscopy

Similar to the XRD technique above, EDS also uses a focused beam of electrons to interact with the surface of the nanopowder placed inside the chamber of the scanning electron microscope. When the electron beam interacts with the surface of the sample, there are secondary electrons expelled from the sample, which gives information concerning the composition of the sample. These secondary electrons are ejected from the orbitals which causes X-rays to be released, and the EDS allows for these X-rays to be collected to determine the characteristics of the sample. The focused beam is primarily used in spot analysis on the surface of a given nanopowder, though it is also used for a scan over a broad portion of the nanopowder surface [32].

The EDS measurements were carried out using EDAX Pegasus system having an Apollo 10 Silico Drift Detector. Data was collected and analyzed using Genesis Spectrum software. The data is presented in the same way as for the XRD, with the counts on the vertical axis and the energy (in keV) on the horizontal axis. These counts provide a chemical analysis of the makeup of the nanopowder. A broad scan and spot scans were used to determine the chemical composition of the nanopowders.

E. Focused Ion-Beam Milling

The focused ion-beam milling process was performed to reveal more information about the cross-sectional structure of the nanoparticles. The sample is mounted in the vacuum chamber shared by both the scanning electron microscope and the energy-dispersive spectrometer, after which an electron gun to emit Ga^+ ions over the surface of the sample being viewed. This ion beam, if focused correctly, will allow for images to be collected of the cross-sectional layers of the sample. As the beam interacts with the surface, a new layer will be exposed, providing a picture of the structural makeup of the sample. This allowed for FIB to verify the information obtained via TEM.

The FIB milling process was conducted with a Focused Ion Beam (FIB) column attached to the Zeiss SEM mentioned above, fitted with a Ga source. Electron beam energy ranged from 10–20 kV. Focused ion beam cuts were made using a Ga^+ ion source with 2 nA/30 kV for the primary cuts and 50 pA/30 kV for polishing cuts.

F. Nanoindentation

To complete a measurement of mechanical properties using quasi-static testing, a finite amount of sample can be mounted in epoxy, where the sample will be subjected to instrumented indentation via a nanoindenter. Using nanoindentation the samples' hardness and Young's Modulus were obtained and plotted accordingly. Using a Berkovich tip, a three-sided pyramid diamond tip (measured and calibrated using a fused silica standard, serial TB15523), there is a known geometry and properties for the tip that would allow us to find out the Young's Modulus and Hardness of the material using the following equations, derived from the Oliver-Pharr Method [45]:

$$\frac{1}{E_r} = \frac{(1-\nu^2)}{E} + \frac{(1-\nu_i^2)}{E_i}$$

Equation 1. Equation to find the Reduced Young's Modulus [45] where E_r is Reduced Young's Modulus and E_i is the Indenter Young's Modulus

$$H = \frac{P_{max}}{A(h_c)}$$

Equation 2. Equation to find the Hardness [45] where P_{max} is the max load, A is the contact area and h_c is the contact depth.

To get the results necessary, the Agilent software was used in the pre-programmed mode for XP-Basic Modulus/Hardness at Depth, this returned the desired Young's Modulus and Hardness. This program operates using quasi-static testing, and as previously establish by Moberg *et al.* [32] the loss modulus for this test with epoxy matrices could be considered negligible. See Table 2.

Calculation Inputs		
% Unload in Stiffness Calculation	50.000	%
Poisson's Ratio	0.400	
Test Inputs		
Allowable Drift Rate	0.0500	nm/s
Depth Limit	2000.000	nm
Peak Hold Time	10.000	s
% to Unload	90.000	%
Strain Rate	0.08	/s

Table 2. Parameters for nanoindentation.

For characterization using nanoindentation, an Agilent Technologies Nano Indenter G200 (see Figure 22) was used to determine the Young's modulus and hardness of the epoxy samples. The nanoindenter used a measurement of the load and displacement into the surface of the material to determine the volume of material displaced by the tip. When the tip was inserted into the material, there is both elastic and inelastic properties; the elastic being the energy that will allow the material to rebound when the tip was removed. The inelastic property was a function of the material that does not rebound once the tip was removed. The information desired was contained in the storage modulus, and thus the elastic energy was the primary focus.

The samples were placed in the sample holder and loaded onto the stage, where the sample was then viewed under an optical microscope to determine correct placement with respect to a standard. Once the placement was established the software was used to program a run of 20 indents, from which the average and standard deviations of the modulus and hardness were calculated [32].

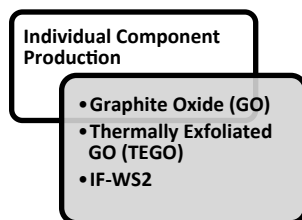


Figure 22. Agilent Technologies Nano Indenter G200 used for characterization via nanoindentation.

IV. RESULTS AND DISCUSSION

In this section the results from testing and characterization will be discussed, as well as the justification for selection of the specific methods used and major findings. In a similar manner as used before, the results will be presented using a graphic diagram to guide the reader through the process, from the synthesis of the individual components to the final generation of the hybrid composite.

A. Individual Components



1. Commercial Graphite Nanopowder to GO to TEGO

Multiple processes for the production of graphene and graphite like sheets and particles have been reported; chemical vapor deposition (CVD) and related methods that generate free-standing graphene sheets [11, 33], thermal exfoliation of graphite oxide [34, 35], and chemical reduction techniques that employ graphite oxide as a precursor and reducing agents such as hydrazine or urea and additives to eliminate oxygen groups [36,37] are some examples.

From the approaches mentioned above, the exfoliation of graphite oxide presents a simple synthetic route that produces higher yields when compared to other options. The method consisted of oxidizing graphite layers to promote a separation between its sheets (sp^2 bond plane, hexagonal honeycomb network typical of graphene) followed by an exfoliation at high temperature. The first step was meant to include oxygen species in between layers, in the form of epoxides or alcohols, while the second would promote their elimination, rendering individual randomly oriented sheets.

As mentioned in the experimental methods, the production of graphite oxide was initially produced using a modified Hummer's method, which called for using commercial graphite flakes as the precursor [8]. Since this research was looking to create large sheets of graphene, the use of graphite flakes would be ideal because the larger our precursor, the greater the likelihood that our final graphene sheets would be large. However, while analyzing the commercial graphite flakes to determine particle sizes by SEM, we found smaller irregular shaped particles from which EDS spectra displayed silicon peaks (see Figure 23). Commercial graphite nanopowder (Sigma-Aldrich, < 20 nm) presented only carbon peaks when studied by SEM EDS and was used as the graphene precursor in all cases.

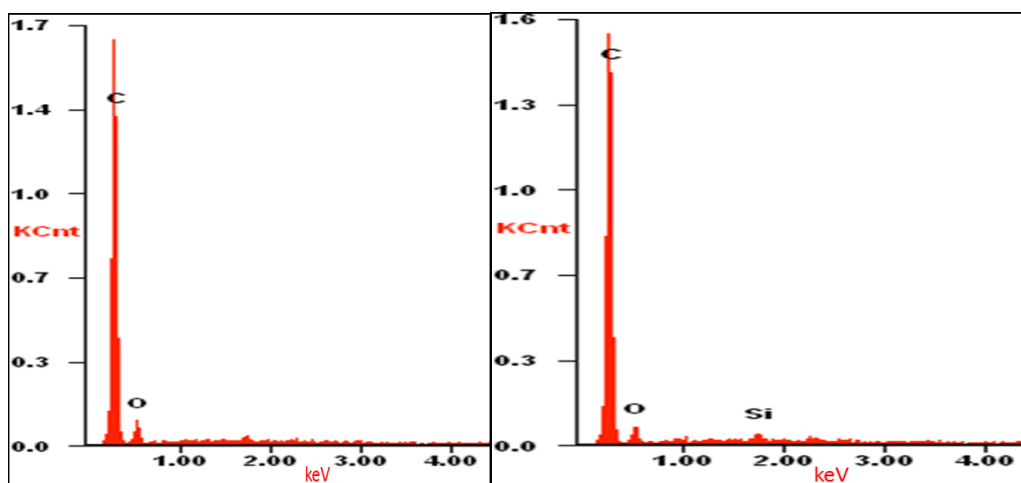


Figure 23. Left) X-ray spectra for GO made from graphite nanopowder Right) Chemical peaks for GO made from graphite flakes, showing silicon impurities.

Figure 24, SEM observation of commercial graphite nanopowder, was representative of the precursor sample, and had a layered microstructure with sheet lengths ranging from 200 nanometers to several micrometers (up to 20 micrometers according to the figure). The sheet thickness appeared to be slightly less than 200 nanometers on average.

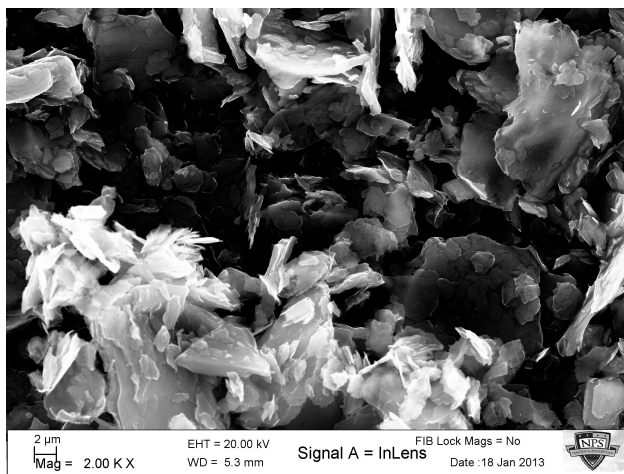


Figure 24. SEM image of Commercial Graphite Nanopowder.

After the production of the GO had been refined to the one listed in the experimental methods, the GO produced was evaluated using XRD, where the d-spacing was calculated using the 2θ values, in order to determine the shifts that occurred during the transformations from commercial graphite nanopowder to GO and finally to TEGO. The respective XRD graphs are presented in Figure 25.

The three more intense peaks for commercial graphite nanopowder were located close to 25, 45 and 55 degrees (2 Theta) and correspond to d values of 3.366 Å, 1.681 Å, and 2.033 Å, miller indices (002), (004) and (101), respectively. The primary indicator we were looking for to know the commercial graphite flakes had transitioned to graphite oxide was the shift of the primary peak from $\sim 25^\circ$ to $\sim 10^\circ$. (Note that the graphs for XRD are given with units of 2 Theta on the x-axis.)

The graphite oxide created from the commercial nanopowder presented peaks close to 10 and 45 degrees (2 Theta), corresponding to d-spacings of 9.100 Å and 2.136 Å. The primary peak in the material, miller index (002), has now shifted from $\sim 25^\circ$ to the near 10° , an indication that the oxide groups have attached to the graphite particles to form the GO. The d value on the graphite oxide sample varies with synthetic method and degree of oxidation and represents the distance in the z direction of the crystal structure of graphite where the oxygen species attach.

The d-spacing for the exfoliated TEGO were 3.681 Å and 6.207 Å, miller indices (002) and (101), respectively. The presence of wide peaks in the XRD pattern, along low intensity peaks, might be interpreted as the TEGO material not being as crystalline as the specimens of commercial graphite nanopowder and GO. Notice that the intensity for the peaks has dropped considerably; the commercial graphite nanopowder had more than 8,000 counts, the GO intensity dropped to around 800 counts, and our finished product, TEGO, had just 60 counts. This drop in intensity, combined with a more noticeable background signal in the samples could indicate a material with less long range order in the z direction and the presence of more defects within the sp^2 layered structure. Furthermore, the most intense peak has shifted from the 10 degrees back to 25 degrees, with the disappearance of the former. This peak shift can be taken as verification that the oxygen groups have been removed from the sample.

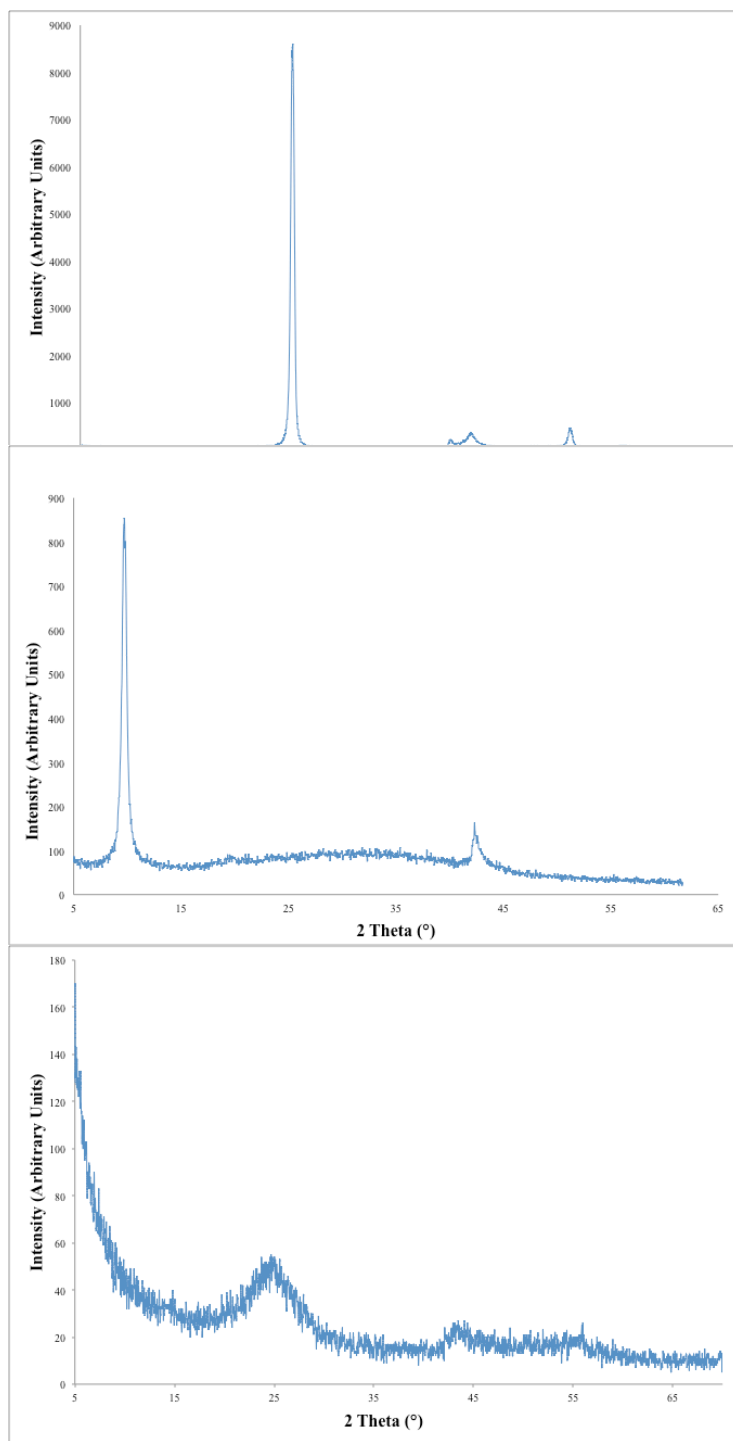


Figure 25. Top) XRD graph for commercial graphite nanopowder Middle) XRD graph for GO Bottom) XRD graph for TEGO

Material	2 Theta (°)	{h j k}	d-spacing (Å)
Commercial Graphite Nanopowder	26.457	(002)	3.366
	54.447	(004)	1.681
	44.067	(101)	2.033
GO	9.718	(002)	9.100
	42.298	(101)	2.136
TEGO	24.613	(002)	3.681
	43.332	(101)	6.207

Table 3. Summary of XRD data for G,GO and TEGO.

The presence of the oxygen species in the GO structure could alternatively be confirmed by spectroscopic techniques as found in the literature [38], although XRD had already provided enough evidence of its inclusion.

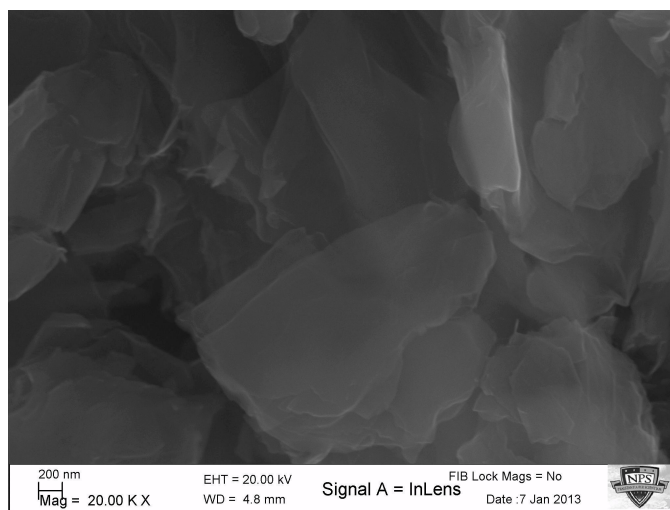


Figure 26. SEM image of graphite oxide.

Compared to the SEM image of the commercial graphite nanopowder (Figure 24), the GO SEM micrographs (Figure 26) showed more space between sheets, indication of the presence of oxygen groups.

Once the exfoliation at high temperature had occurred, the TEGO produced presented the morphological characteristics illustrated in Figure 27.

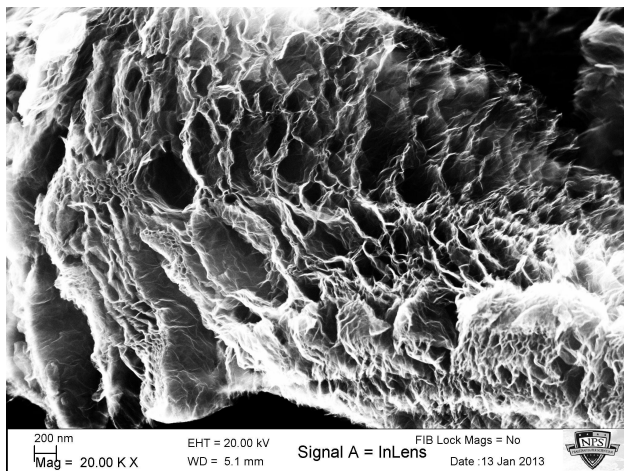


Figure 27. SEM image of Thermally Exfoliated Graphite Oxide.

Rather than individual sheets, the material exfoliated in a direction perpendicular to the sheet orientation, exhibiting a splayed edge in what could be called a honeycomb type structure. It is worth noting that this microstructure shares characteristics with the honeycomb structures commonly used in radiation absorbing foams. Each fan-shaped structure could reach length in the micrometer range, and does not present any relative orientation with respect to each other.

This lack of uni-directional orientation may provide both the necessary structure and flexibility allowing the material to behave with more rigidity while still being able to maintain the movement characteristic of graphene sheets. If the morphology found were individual graphene sheets, this would allow the sheets to slide into one another when impacted.

2. IF-WS₂

Many fabrication methods have been proposed and tested to generate inorganic fullerene type tungsten disulfide particles. These include, but are not limited to, electron-beam irradiation activation, arc discharge, thermal decomposition, hydrothermal or solvothermal synthesis, sonochemical process, sublimation-condensation technique, laser

ablation, template synthesis, and combinations thereof [21, 23]. By far the most used come from solid-gas or gas phase reactions performed inside of tube furnaces. In such scheme, a sample containing tungsten oxide or halide is placed in a boat inside the oven and subjected to a sulfur rich environment. Due to the increased heat the tungsten material reacts with the sulfur and forms tungsten disulfide. The first of the solid-gas processes, was used by Tenne et al. and led to the discovery of IF-WS₂, consisted of heating tungsten oxide in N₂+H₂+H₂S atmospheres at 850°C. The process was relatively simple, relying on only one reaction to take place: the sulfurization of the tungsten around the oxide template in an outside-in process. The particles created from this process were reported to be between 90 and 120 nm on average [39].

Throughout the many experiments performed on IF structures, it has been found that the inorganic fullerene characteristics depend to a large extent on the nature and morphology of the precursor. The shape and size of the precursor particles readily forecast the general shape and size of the IF products. In the outside-in formation process, the size and shape is determined by the first formed layer of WS₂. Being able to control the precursor morphology would be one possible way to ensure consistent products and is the reason why this thesis has undertaken such task. The IFs are thermodynamically stable structures only when synthesized below certain temperatures and reaction times. A range of particles are formed at different temperatures, beyond a particular window of conditions the particles take the form of the macroscopic platelets, phase commonly found when bulk WS₂ is finely ball milled. Finely grinding WS₂ is the easiest way to obtain nanometric WS₂ although such phase does not have the desired properties found in IFs.

We attempted to generate IF-WS₂ from ammonium tetrathiotungstate, commonly referred to as an ammonium salt, and from commercial WO₃. Given that the commercial particulate morphology in the latter case was difficult to control, we used a third approach where the ammonium salt was employed as a precursor to generate spherical WO₃ by plasma methods, which was then converted to IF-WS₂ by a sulfurization step. The next sections summarize our findings.

a. WS₂ from Ammonium Tetrathiotungstate Salts

The use of ammonium tetrathiotungstate as a precursor for the WS₂ represented a facile route for producing WS₂ since its thermal decomposition generates directly the targeted solid product. The crystal structure of the powders was studied by X-ray diffraction methods and their morphology by Scanning Electron Microscopy. In the former, the main peaks of the WS₂ structure could be identified, although despite changing the acquisition rates of the spectra, only very low intensity peaks were detected, indicating a product with low crystallinity.

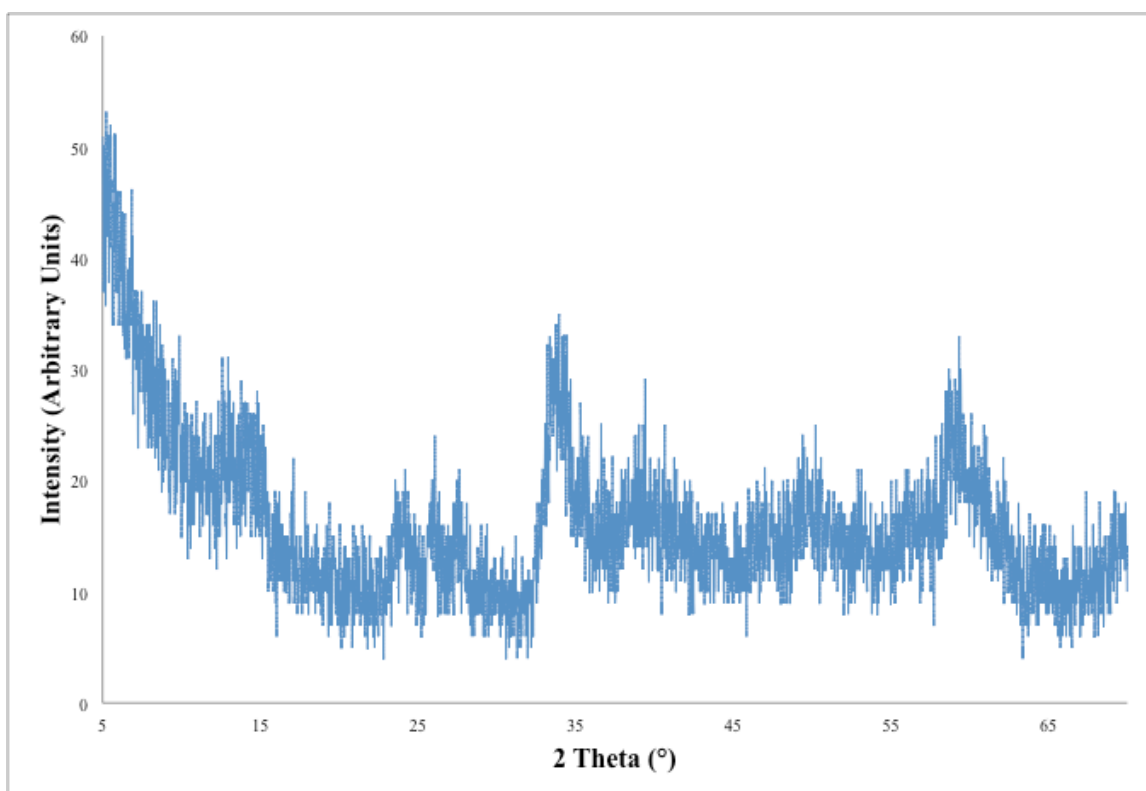


Figure 28. XRD graph of WS₂ from salts.

The values for the d-spacings of the main peaks (see Figure 28) correspond to 2.640 Å, 1.557 Å and 2.286 Å, miller indices (101), (110) and (002) respectively. SEM examination of the sample revealed large agglomerates combined with submicron particles, with only few of them presenting semi-spherical WS₂ shapes (see Figure 29 Left and Right).

Material	2 Theta (°)	{h j k}	d-spacing (Å)
WS ₂ from Salts	33.748	(101)	2.640
	59.337	(110)	1.557
	14.158	(002)	2.286

Table 4. Summary of XRD data for WS₂ from salts.

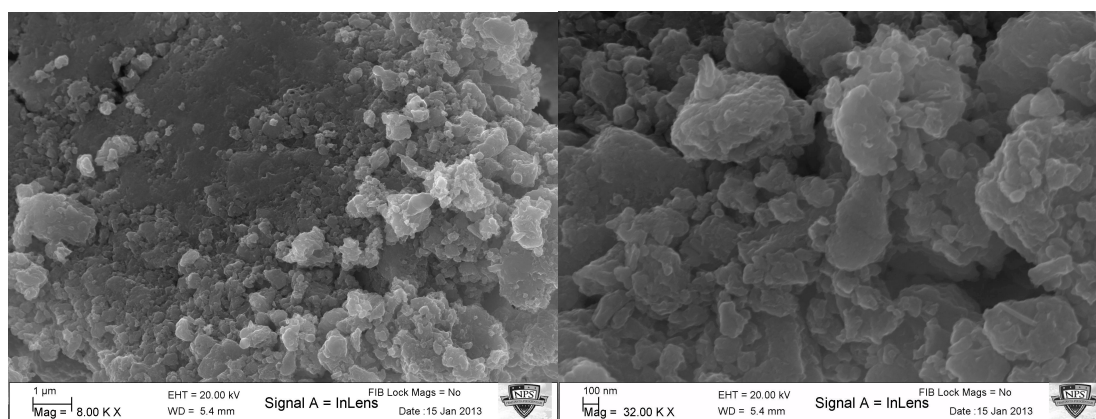


Figure 29. Left) SEM image of WS₂ from (NH₄)₂WS₄ Right) SEM image of WS₂ from (NH₄)₂WS₄

b. WS₂ from WO₃ Commercial

As mentioned before, tungsten oxide has been successfully used to produce particles with IF-WS₂ morphologies when the precursor size is adequate. However, commercial WO₃ nanoparticles purchased from different vendors contain a myriad of particle sizes, and it is only through ball milling processes or finely grinding with a mortar that consistent submicron sizes can be generated. Bulk WO₃ exhibits a series of polymorphs, which can be conveniently described as deviations from the ideal cubic ReO₃ structure. At room temperature, the WO₃ structure is monoclinic (c-WO₃ phase with space group P2₁/n) and can be approximated by a distorted (2x2x2) arrangement of the ideal ReO₃ type unit cells. The lattice parameters for this phase are a=7.297Å, b=7.539Å, c=7.688Å, and β=90.91 [16].

Analysis of crushed powders by XRD (see Figure 30) presents the typical pattern for WO_3 just described, with the main peaks located close to 25 and 35 degrees and multiple smaller intensity peaks.

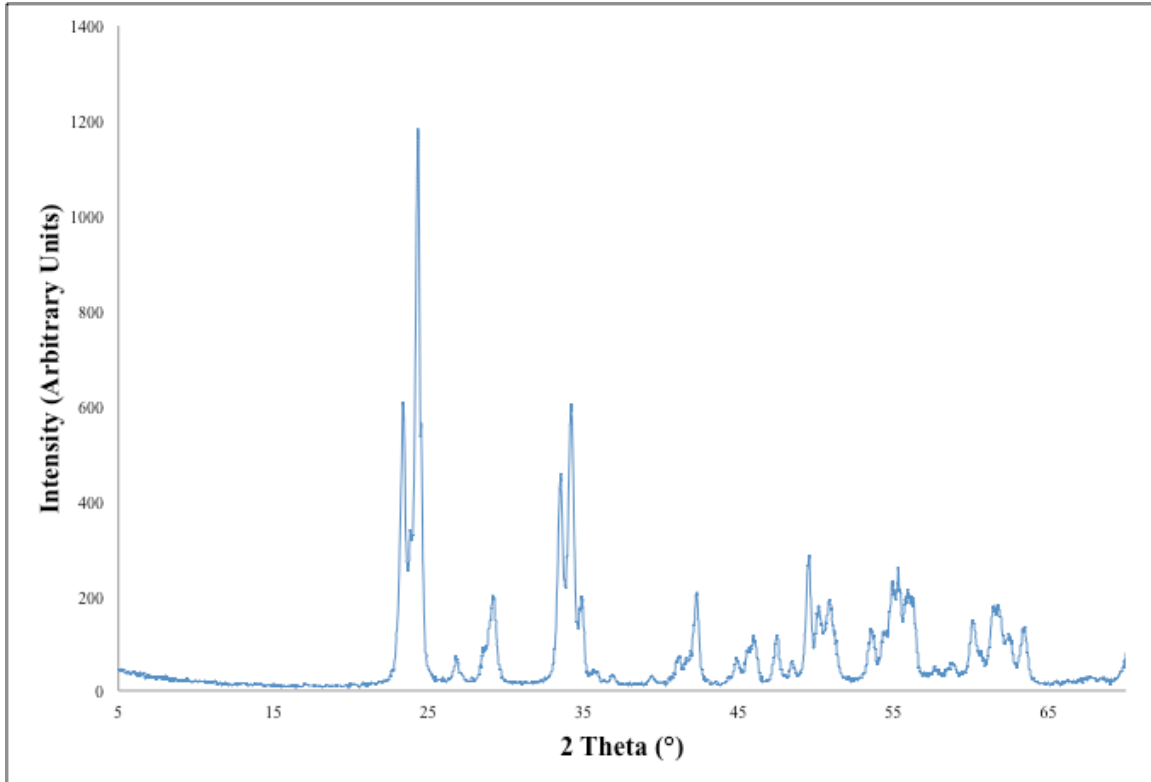


Figure 30. XRD graph for WO_3 commercial.

The values for d-spacing are 3.680 Å, 3.840 Å and 2.636 Å, miller indices (200), (220) and (021) respectively. The sharp peaks illustrate the highly crystalline nature for this particular sample.

Material	2 Theta (°)	{h j k}	d-spacing (Å)
WO_3 Commercial	24.328	(200)	3.680
	34.183	(220)	3.480
	23.338	(021)	2.636

Table 5. Summary of XRD data for WO_3 commercial.



Figure 31. SEM image of hand crushed WO_3 commercial.

The SEM was used to verify the shape of the WO_3 particles (see Figure 31); there are two primary shapes we viewed for the WO_3 , an angular semi-trapezoidal shape, and the desired spherical shape, which would give rise to the IF- WS_2 particles that are the desired end product.

In any case, the particles were sulfurized for a period of 3 hours to generate IF- WS_2 . The expected process will follow the outside-in front to convert the outer layers first and then evolve towards the particle interior. Despite a large treatment time, the sample XRD patterns retain some of the original WO_3 peaks (located close to 25 degrees). The rest of the spectra are consistent with a well crystalized WS_2 structure. See Figure 32. This result constitutes evidence the presence of WO_3 in the WS_2 product and could be explained by the outer layers of the particles being sulfurized and preventing more sulfur to diffuse into the particle core to completely react, leaving a trace of oxide inside.

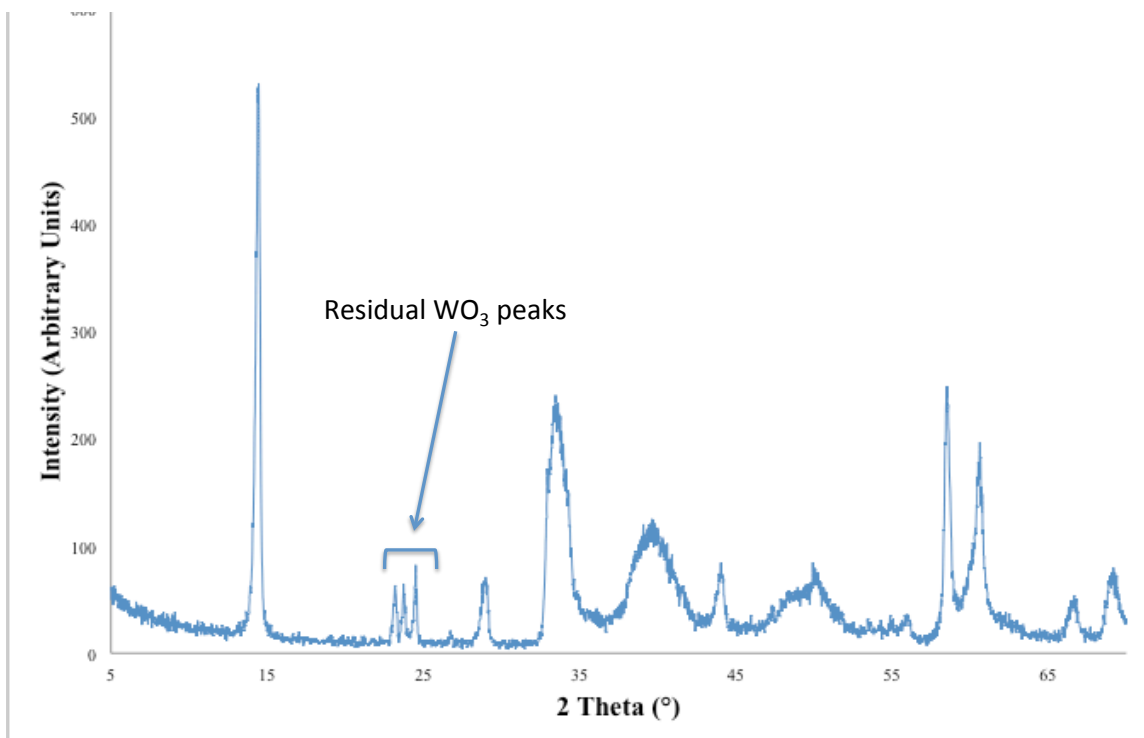


Figure 32. XRD graph of WS_2 from WO_3 commercial that shows the presence of WO_3 after sulfurization.

The d-spacing values are similar, though shifted from those found in the WS_2 produced from $(\text{NH}_4)_2\text{WS}_4$, where the peak values represent d-spacing of 6.138 Å, 1.577 Å and 2.680 Å, miller indices (002), (101) and (008), respectively.

Material	2 Theta (°)	{h j k}	d-spacing (Å)
WS ₂ from WO ₃ Commercial	14.398	(002)	6.138
	58.512	(101)	1.577
	33.343	(008)	2.680

Table 6. XRD data for WS_2 from WO_3 commercial.

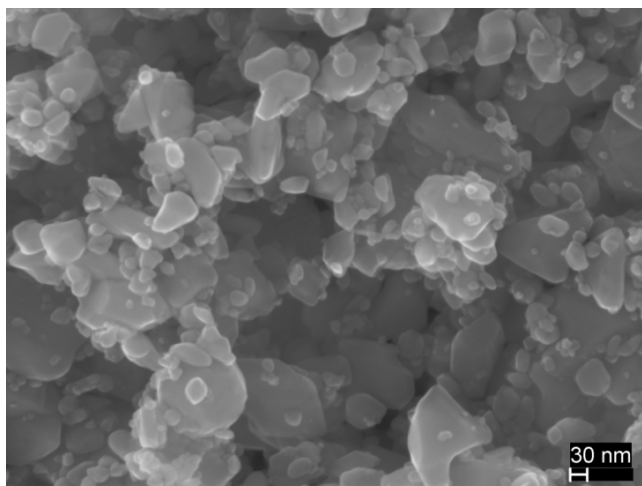


Figure 33. SEM image for WS_2 from WO_3 commercial.

SEM images of the converted phase reveals that particles have irregular or semispherical shapes (see Figure 33). The particle size distribution for this sample is presented in Figure 34, with a calculated average particle diameter of 102.6 nm and a minimum size of 10.3 nm and a maximum size of 871.7 nm.

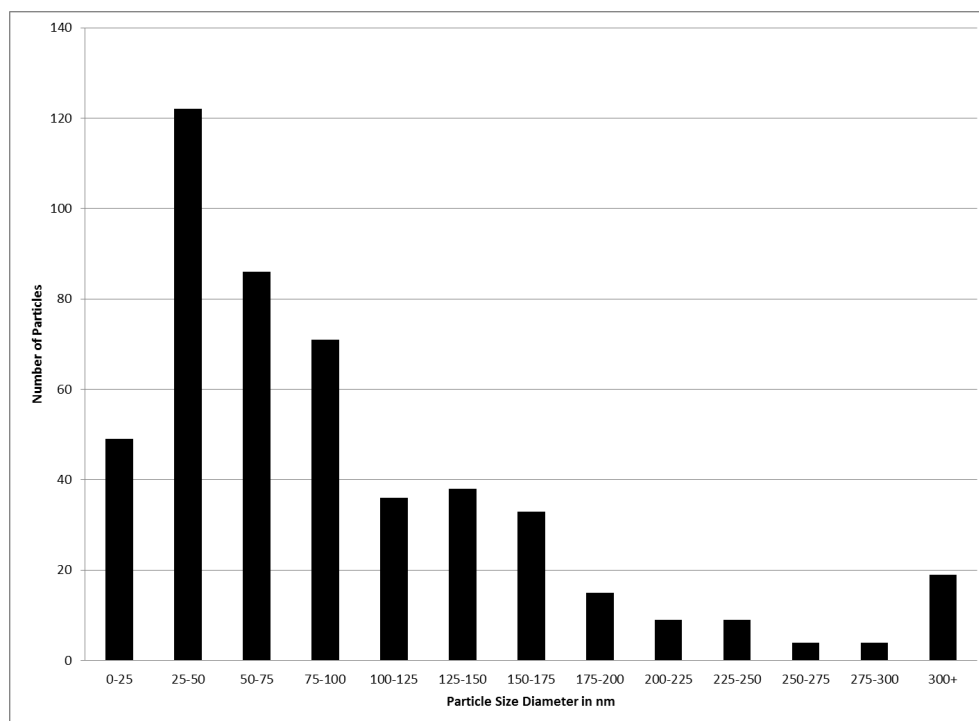


Figure 34. Histogram for particle size distribution for WS_2 from WO_3 commercial.

The data above shows that 76.5% of the WS₂ produced in this sample was ≤ 200 nanometers. However, the goal was to achieve a sample at or close or below 100 nanometers that exhibits the spherical shape of the desired IF-WS₂. Nevertheless, the result is a positive one since it is very close the one reported in the literature of 90–120 nm. [40]

c. WS₂ from WO₃ Plasma

A closer look at the commercially available plasma related methods will include materials deposition, removal, patterning and modification of its electrical properties. Plasma techniques based on argon or oxygen discharges are responsible for the generation of Al, W and superconducting films, while oxygen discharges have been utilized to grow Si, Si₃N₄ and SiO₂ films. Boron halide discharges are used for B implantation in silicon and diverse compositions (i.e., CF₄, O₂, Cl₂) used to selectively remove silicon films. Oxygen discharges can also remove photoresist and activate diverse surfaces, even promote polymerization processes. For the micro-fabrication of an integrated circuit a considerable amount of steps involve some kind of plasma based technology. In contrast with the thin film fabrication, the approaches to generate particulate and free standing materials are not usually focused on plasma methods. Apart of the creation of “islands” and clusters by sputtering techniques, usually grown to eventually form extended films, plasma based methods have found a niche at the thin film technology industry and have opened a way to other techniques, such as the ones based on colloids, microemulsions and sol gel approaches for approaches for particles and free phases generation.

NPS creates plasmas using an aerosol through microwave plasma system that operates at or close to atmospheric pressure, which has been used to generate micron and nanoparticles for catalyst, sensors, batteries, propants and other applications. From metallic, alloy, oxides, complex oxide systems to composite carbon/metal, oxides/carbon and combinations of oxides with different properties [15, 21, 39,40], along with homogeneous dispersions metal/matrices, our team has been able to combine phases at a micron and nanometer scale with targeted structures/properties for specific applications.

Such previous work supports the idea that using atmospheric plasma approaches one can control nanostructure characteristics, including morphology, crystal structure and amount of oxygen surface groups. Precursor composition, flow rates, for carrier and plasma gases, generator power and pressure exhaust are common factors that can be modified to tune product features.

The plasma system offers new exciting possibilities for materials preparation, is versatile due to the multiple variables that can be controlled. One can also add to the particularities of the system the inherent complications (and potential) of plasma discharges: very high temperatures (ca. 2000–3000 degrees C), generation of radicals and the existence of neutral and charge species at different temperatures in a confined system.

The shift from using commercial WO_3 to an in-house created WO_3 generated using the plasma torch was prompted by the overly large particle size of the commercial WO_3 mentioned above. The material created using the plasma method proved to be more spherical, keeping the inorganic fullerene shape, and contained smaller average particle size.

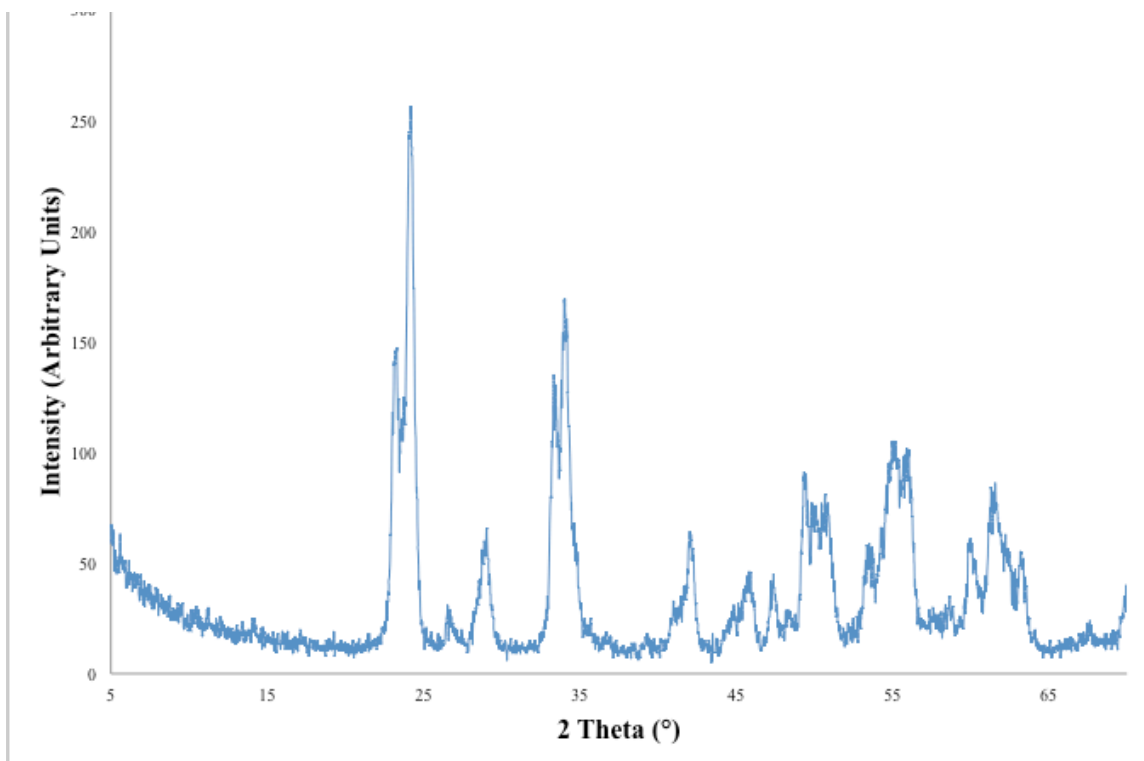


Figure 35. XRD graphs of WO_3 from plasma.

The values for d-spacing are very similar to those for WO_3 commercial; the values are 3.682 Å, 2.631 Å and 1.846 Å respectively (see Figure 35). We have the primary peak located $\sim 25^\circ$, and the material peaks indicated the crystalline nature of the material generated.

Material	2 Theta (°)	{h j k}	d-spacing (Å)
WO_3 from Plasma	24.178	(200)	3.682
	34.003	(220)	2.631
	23.113	(021)	1.846

Table 7. XRD data for WO_3 from plasma.

The SEM was used to confirm the more spherical shape of the WO_3 particles produced using the plasma torch (see Figure 36). Initial estimates by visual

inspection showed great promise, with less than 1% of the material appearing to be non-spherical in nature.

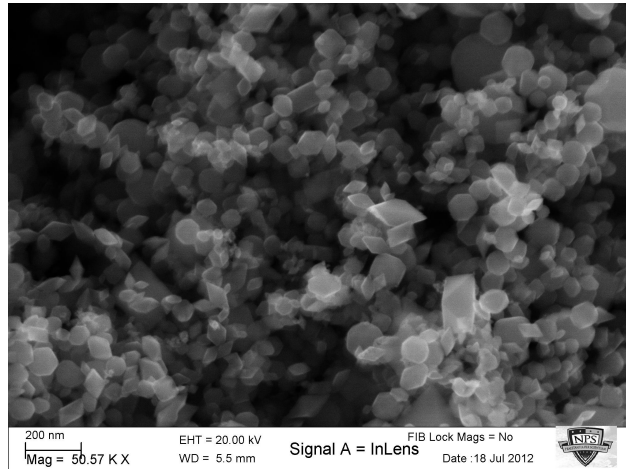


Figure 36. SEM image of WO_3 from plasma.

The spherical particles were generated in much larger quantities, though there was still a small amount of trapezoidal shaped WO_3 particles produced. From the SEM, a particle size distribution was obtained by using hand calculation via ImageJ software. For comparison with other images, an image at 32Kx magnification was used (see Figure 37).

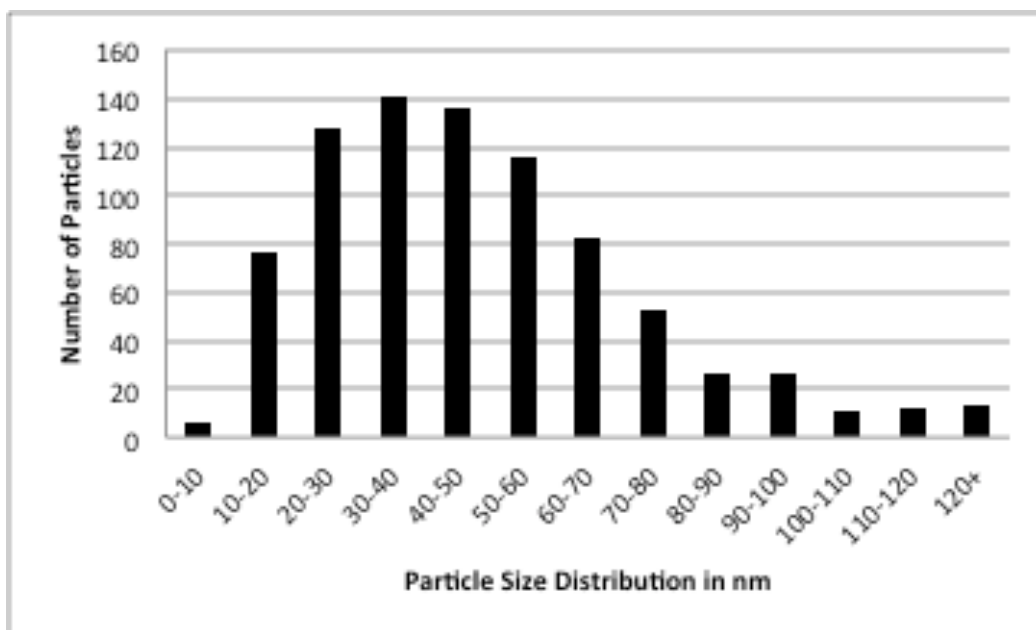


Figure 37. Histogram of WO₃ plasma Particle Size Distribution.

From the measurements on ImageJ, the average particle size was 49.3 nm, with a minimum particle size of 5.1 nm and a maximum particle size of 356.7 nm, and as seen in the histogram, 86% of the particles were ≤ 75 nm. This size more than exceeds the desired particle size of 100 nm, while keeping the inorganic fullerene type structure.

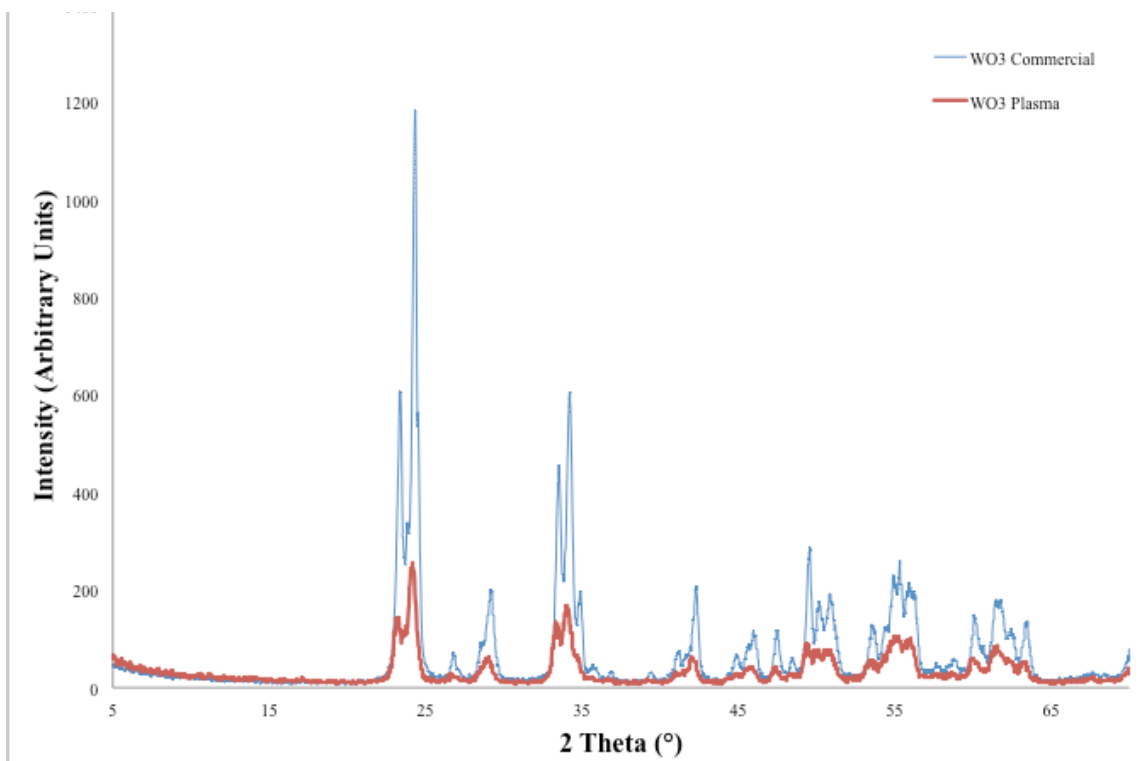


Figure 38. XRD graph of combined WO₃ commercial and plasma.

Figure 38 provides a means for comparison between WO₃ generated via plasma methods, and the WO₃ that is available commercially. The sharper peaks for the WO₃ commercial are a good indication the particles contain facets less than 90 degrees, whereas the less steep peaks for the WO₃ plasma indicate a more spherical particle has been generated.

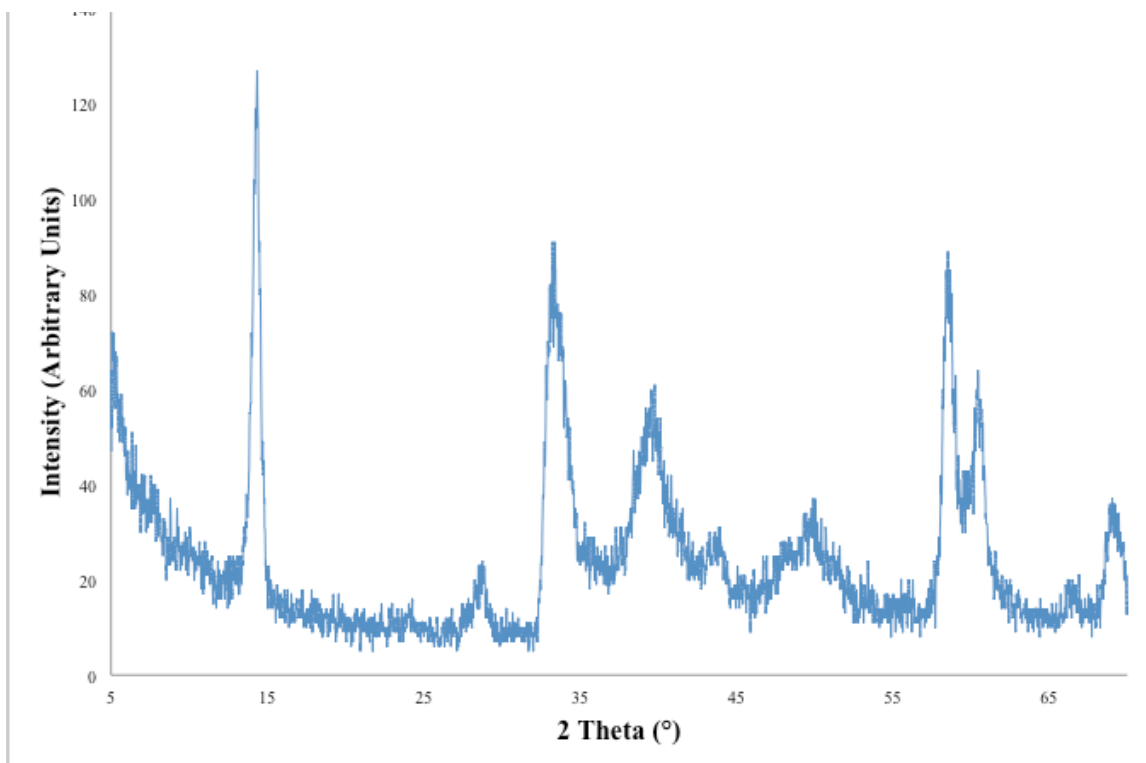


Figure 39. XRD graph of WS₂ produced from WO₃ plasma.

The XRD pattern presented in Figure 39 illustrates peaks that can only be associated to WS₂; there are no peaks indicating a remaining presence of WO₃. This complete sulfurization of the material to WS₂ means a hollow core was left behind where there previously was WO₃. These peaks are very similar to those from the WS₂ produced from WO₃ commercial; however, the intensity of the 2nd and 3rd peaks is switched. The d-spacing is 7.051 Å, 2.695 Å and 1.580 Å, respectively.

Material	2 Theta (°)	{h j k}	d-spacing (Å)
WS ₂ from WO ₃ Plasma	14.338	(002)	7.051
	33.328	(101)	2.695
	58.512	(110)	1.580

Table 8. XRD data for WS₂ from WO₃ plasma

The main difference among plasma and commercial WO_3 particles transitioned into WS_2 is that the ones from plasma do not show any remnant WO_3 but a single phase, indication that the reaction continued to completeness and there was no WO_3 left in the particle cores. The combined XRD graph is displayed below (see Figure 40), and it provides excellent contrast between the peaks of the differing WS_2 samples. This makes it clear that the WS_2 commercial has the sharper and more intense peaks, which also indicates that the material is more crystalline. The WS_2 from salts looks like noise when compared to that of the WS_2 commercial and WS_2 plasma—this is due to the lack of crystalline particles from this sample. The WS_2 plasma has peaks with the intensities that indicate the material is crystalline, though not as steep as the WS_2 commercial. The inset in the figure clearly shows a shift to lower angles for the peak located close to 14 degrees (14.10 degrees) in the sample generated from plasma precursor when compared to the one from commercial WO_3 particles. This shift has been associated with the IF- WS_2 particular structure and it is correlated to a different distance between sulfide layers due to an internal strain created as the material sheets curve around to form a spherical particle [30]. Such a shift in the (002) reflection of the hexagonal structure of IF- WS_2 is a strong evidence of a successful completion of process to fabricate the desired IF- WS_2 . The peak from commercial particles is closer to the spacing observed in the two-dimensional WS_2 crystals.

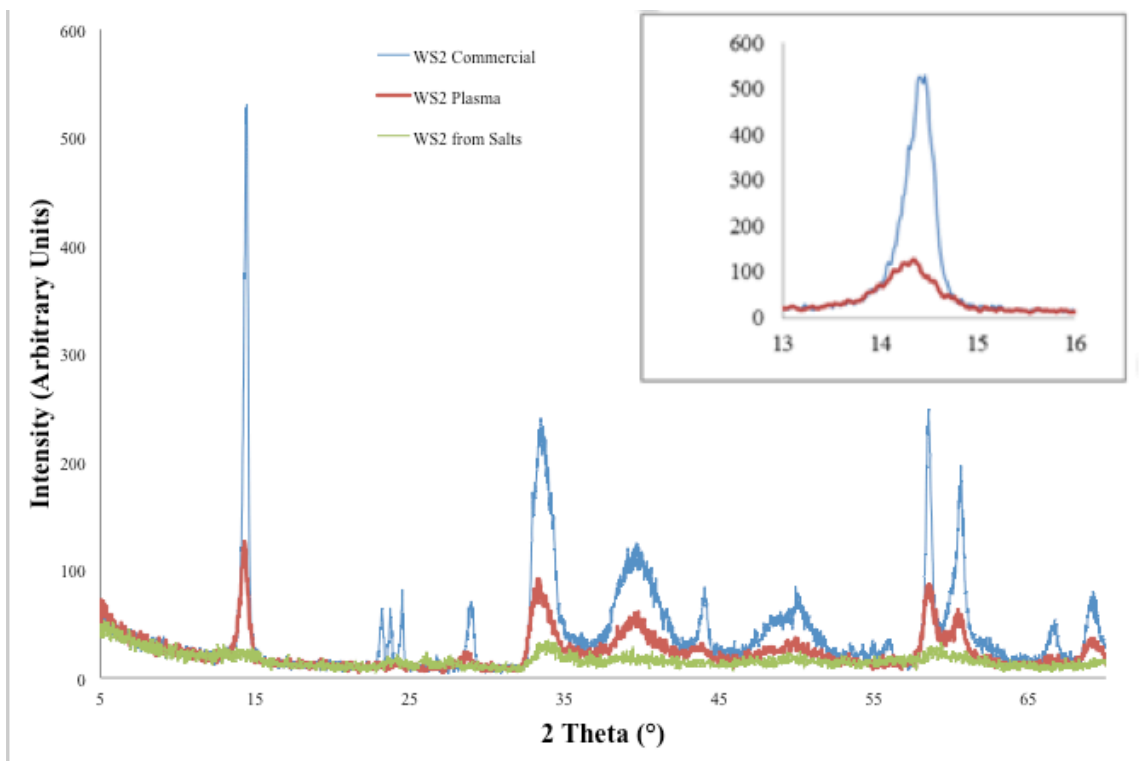


Figure 40. Combined XRD graph of WS₂ with inset of WS₂ commercial and WS₂ plasma at 14° to show 2 theta shift.

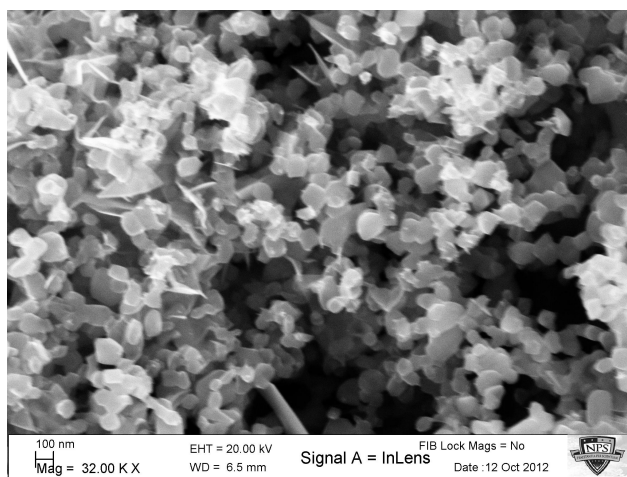


Figure 41. SEM image of WS₂ from WO₃ plasma.

The SEM images of the WS₂ in Figure 41 confirmed that the production via plasma torch was more effective at producing the desired IF-WS₂. The average

particle diameter (see Figure 42) was 88.4 nm, with a minimum particle size of 24.0 nm and a maximum particle size of 24.0 nm, which exhibits the desired particle size of ≤ 100 nanometers. A histogram was generated to reveal that 69.97% of the particles were ≤ 100 nanometers.

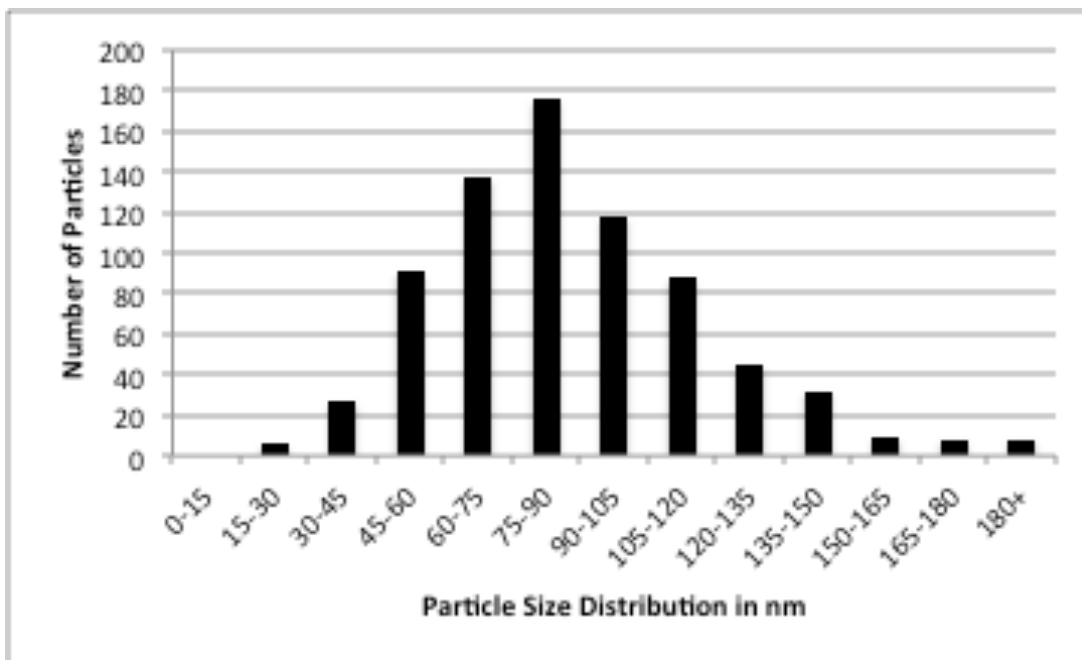


Figure 42. Histogram of WS₂ plasma particle size distribution.

The IF-WS₂ exhibited a size increase of 44.2%, increasing in average diameter from 49 nm to 88 nm, though the results were favorable as the overall particle diameter was under the 100 nm threshold. After the particles were analyzed using SEM, they were studied further with TEM to confirm the IF-WS₂ structure's presence. Images of the agglomerated particles were collected (see Figure 43), as well as singular images of both the spherical IF-WS₂ and the semi-trapezoidal ϵ -WS₂

Although spherical and semispherical particles dominate the microstructure of the sample, in the conditions of synthesis used, a small fraction of WS₂ possessing a single sheet morphology, analogous to graphene in carbon, was produced.

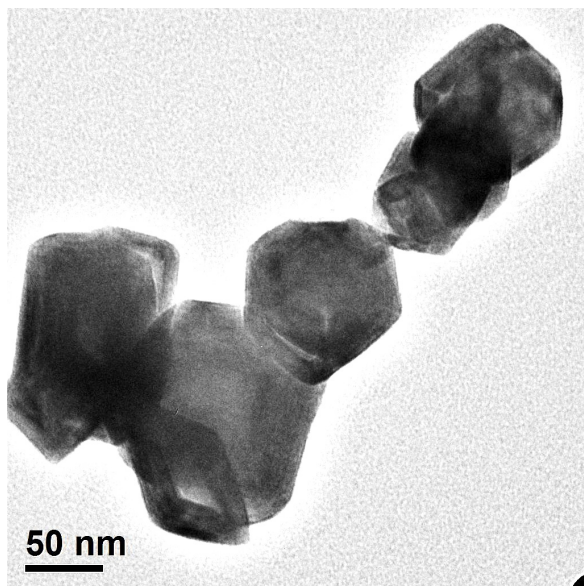


Figure 43. TEM image of WS_2 cluster.

It should be noted in the image above that the cluster is comprised primarily of the IF- WS_2 particles, but there is the presence of the trapezoidal ϵ - WS_2 , which is shown in greater detail in Figure 44.

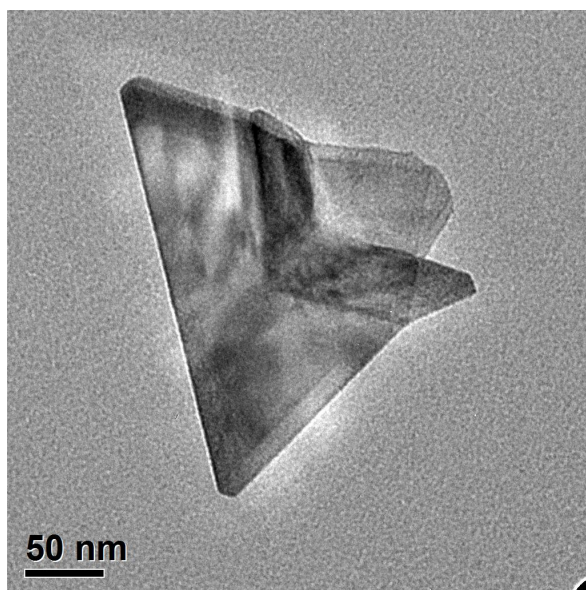


Figure 44. TEM image of WS_2 plasma showing an isolated non-spherical WS_2 .

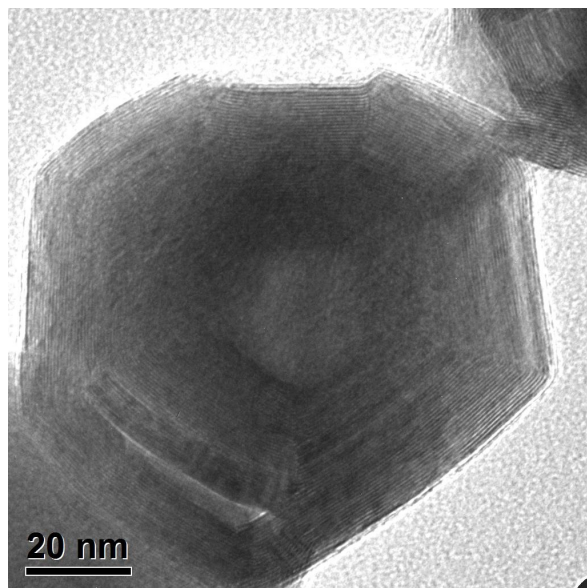


Figure 45. TEM image of WS_2 plasma showing IF- WS_2 .

Figure 45 shows the creation of our IF- WS_2 from plasma achieves the shape of spherical or polyhedra, hollow cores with a layered structure. The angles of the edges are greater than 90° , similar to particles which have been able to withstand shock pressures at or greater than 25 GPa [41].

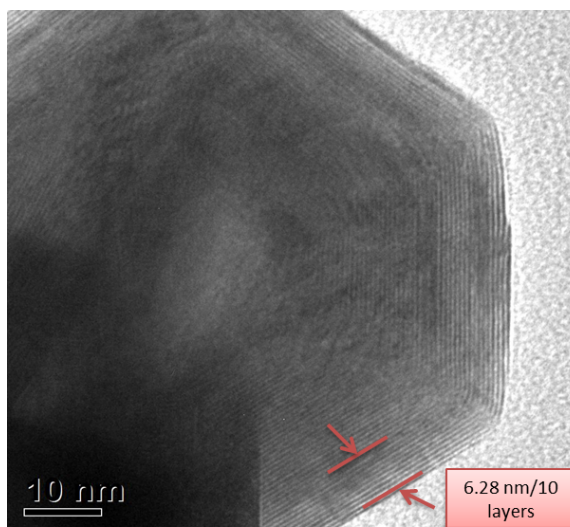


Figure 46. TEM image of WS_2 plasma used for gap spacing measurements.

The spacing between the layers (see Figure 46) was calculated by hand using ImageJ, where the total spacing for ten layers, plus gaps, was 0.628 nm, which confirms the lattice separation of highly strained layers typical of IF-WS₂ previously identified by XRD.

In Figure 47, images from FIB milling use arrows to highlight the presence of hollow cores, which can be seen as the lighter line seen on the particles, and is particularly noticeable for the particle in the center of the 64s image.

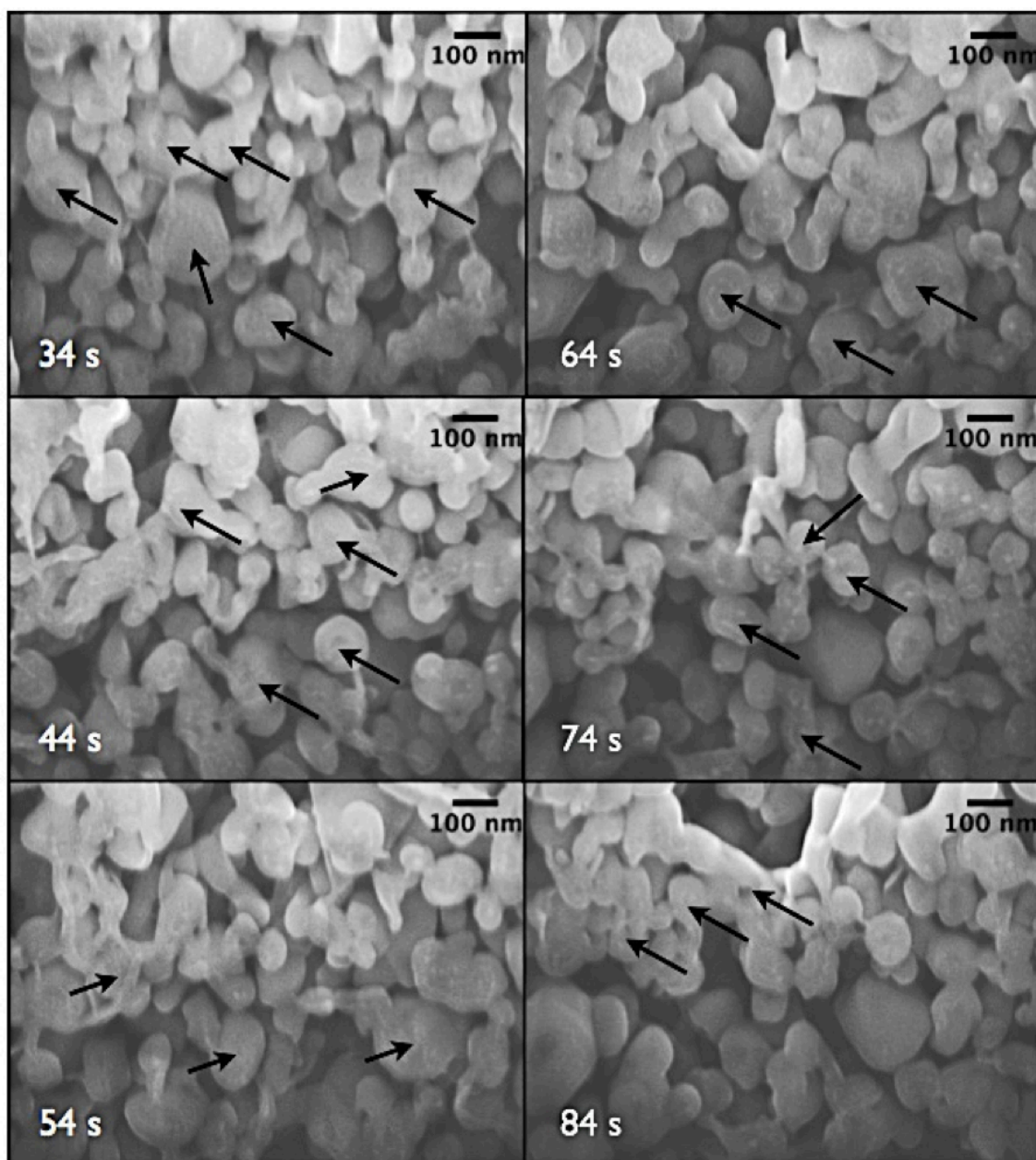
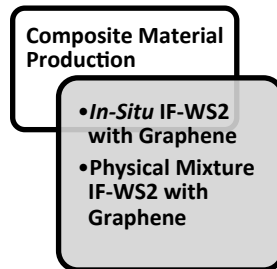


Figure 47. Focused Ion Beam Milling was used to remove layer by layer to show the existence of hollow cores (indicated by arrows in some particles) as a consistent feature in the IF-WS₂ sample produced from plasma WO₃ precursor.

B. Hybrid IF-WS₂ and Graphene

The hybrid composites were designed with a 99:1 ratio of graphene to IF-WS₂, which was established through research conducted by ENS Mike Moberg [32]. Once the hybrids were created, the samples were evaluated for exact chemical composition using

atomic absorption at the University of New Mexico, which revealed one sample to contain an actual ratio of 99.5:0.5 and the other to contain a ratio of 98.5:1.5.



1. *In-Situ* Hybrid IF-WS₂ and Graphene

a. *In-Situ Hybrid from (NH₄)₂WS₄ and TEGO*

Using both XRD and SEM, the material was characterized, and established a baseline for the hybrids.

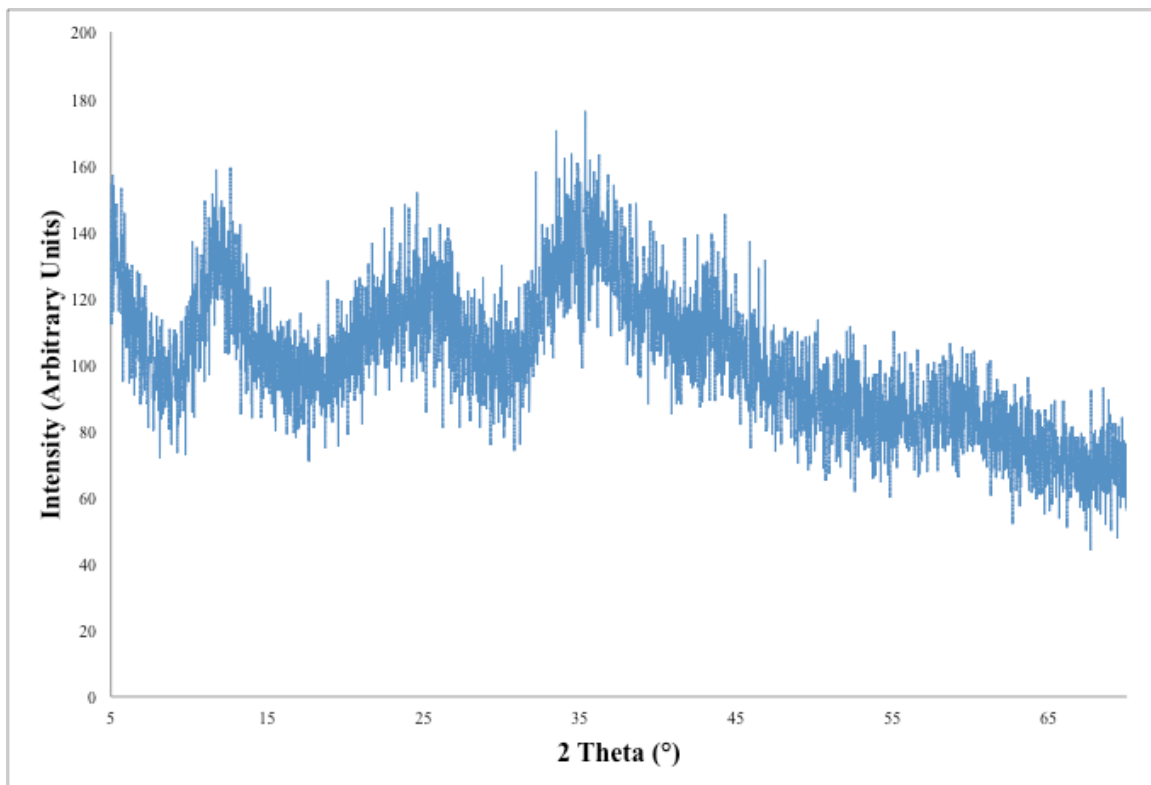


Figure 48. XRD graphs of *in-situ* IF-WS₂ and graphene from salts.

For Figure 48 the d-spacing was calculated as 2.539 Å, 7.538 Å and 3.619 Å, miller indices WS₂ (103), WS₂ (002) and G (002), respectively. We see the peaks indicating the presence of both the graphene and the WS₂. However, from the production of the WS₂ from the ammonium tetrathiotungstate, we know that this material does not contain the desired IF-WS₂.

Material	2 Theta (°)	{h j k}	d-spacing (Å)
<i>In-Situ</i> IF-WS ₂ and Graphene from Salts	35.350	WS ₂ (103)	2.539
	11.490	WS ₂ (002)	7.538
	24.550	G (002)	3.619

Table 9. XRD data for *in-situ* IF-WS₂ and graphene from salts.

b. In-Situ Hybrid from IF-WS₂ Plasma and TEGO

This material was synthesized and then characterized using both XRD and SEM; these results were used for comparison to determine whether or not the material met the desired requirements of having both the graphene sheets and the IF-WS₂.

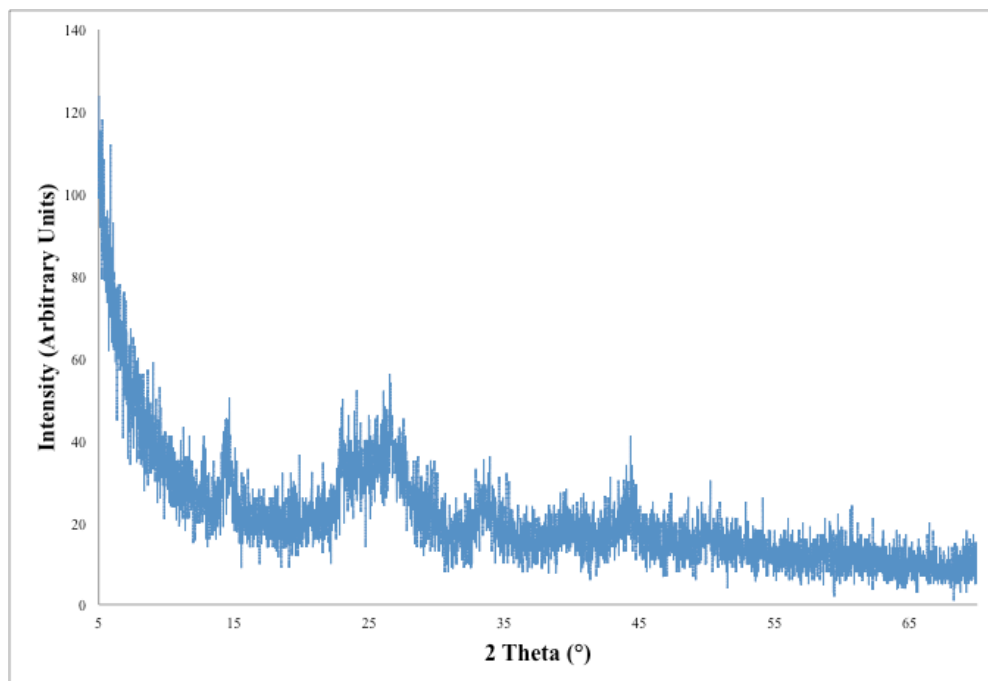


Figure 49. XRD graphs of *in-situ* IF-WS₂ and TEGO.

These graphs were used to obtain the d-spacing, which were broken down in order of peak intensity and are 3.360 Å, 6.038 Å and 2.043 Å, miller indices G (002), WS₂ (002) and WS₂ (101) respectively. In the XRD seen in Figure 49, we again see the peaks showing the presence of the graphene and the peak for IF-WS₂, while also seeing the disappearance of the oxygen groups.

Material	2 Theta (°)	{h j k}	d-spacing (Å)
<i>In-Situ</i> IF-WS ₂ and TEGO	35.350	WS ₂ (103)	2.539
	11.490	WS ₂ (002)	7.538
	24.550	G (002)	3.619

Table 10. XRD data for *in-situ* IF-WS₂ and TEGO.

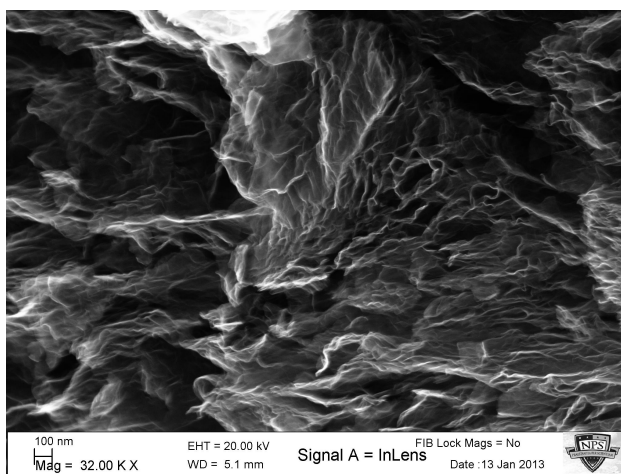


Figure 50. SEM image of hybrid from WS₂ plasma and TEGO.

The SEM verified that the graphene sheets were adequately exfoliated to provide the desired spacing between the sheets (see Figure 50 and 51). As well, the spherical IF-WS₂ was dispersed throughout the composite. We did see aggregates of IF-WS₂, though these appeared to be random homogeneous dispersions located at the edges of the graphene sheets.

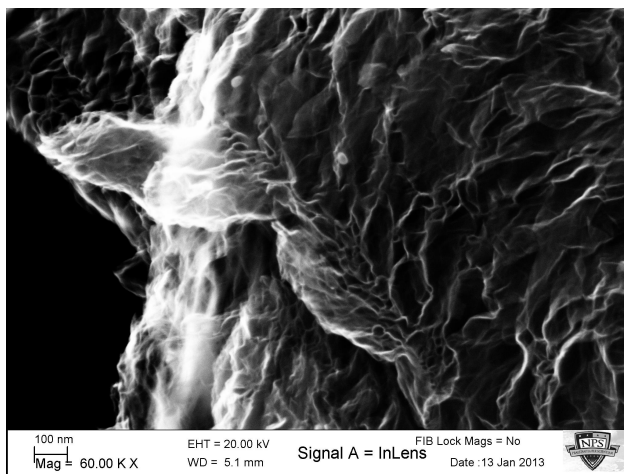


Figure 51. SEM image of hybrid from WS₂ plasma and TEGO.

2. Physical Mixture Hybrid IF-WS₂ and Graphene

This mixture was also analyzed using XRD and SEM.

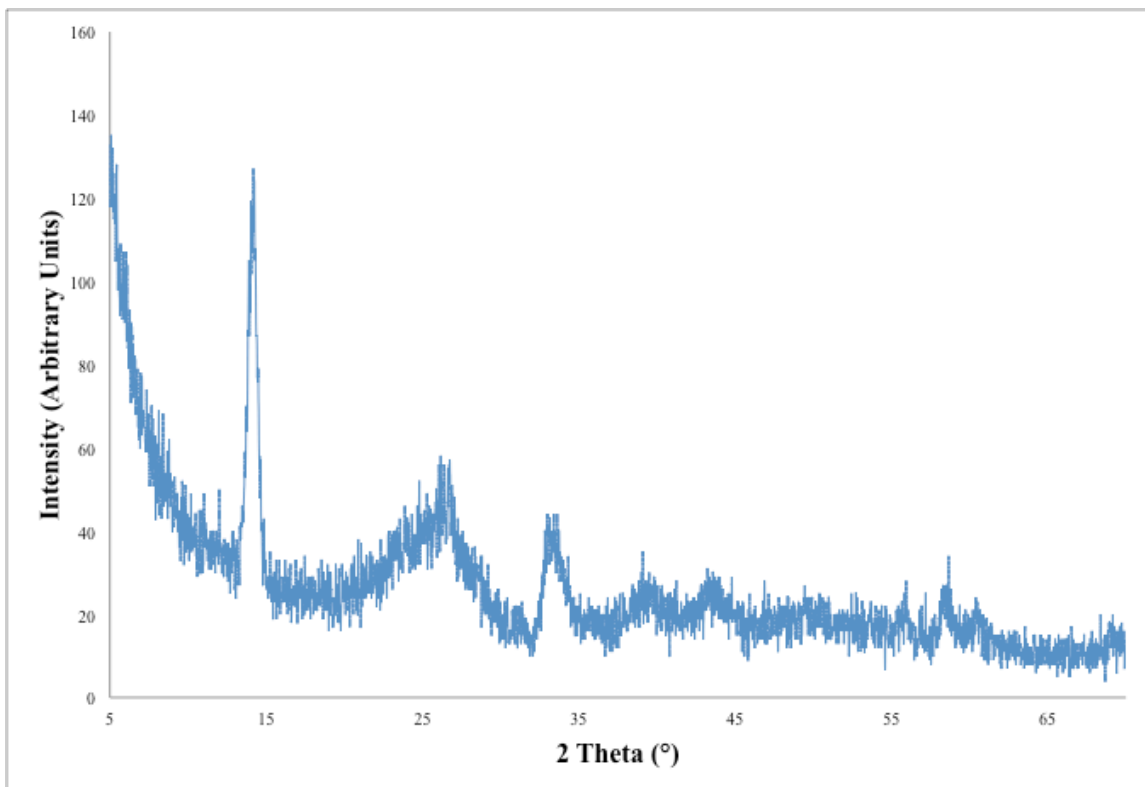


Figure 52. XRD graphs of physical mixture hybrid.

The d-spacing was calculated using Bragg's Law and determined in respective order of peak intensity and is 6.312 Å, 3.407 Å and 2.715 Å, miller indices WS₂ (002), G (002) and WS₂ (101) (see Figure 52). These values are similar to that above for the *in-situ* hybrid composite, which showed the presence of the graphene and the IF-WS₂ although the intensity of the peaks is higher and each reflection in the spectra is more defined as illustrated in Figure 53.

Material	2 Theta (°)	{h j k}	d-spacing (Å)
Physical Mix IF-WS ₂ and Graphene from Salts	14.173	WS ₂ (002)	6.312
	26.053	G (002)	3.407
	36.968	WS ₂ (101)	2.715

Table 11. XRD data for physical mixture hybrid.

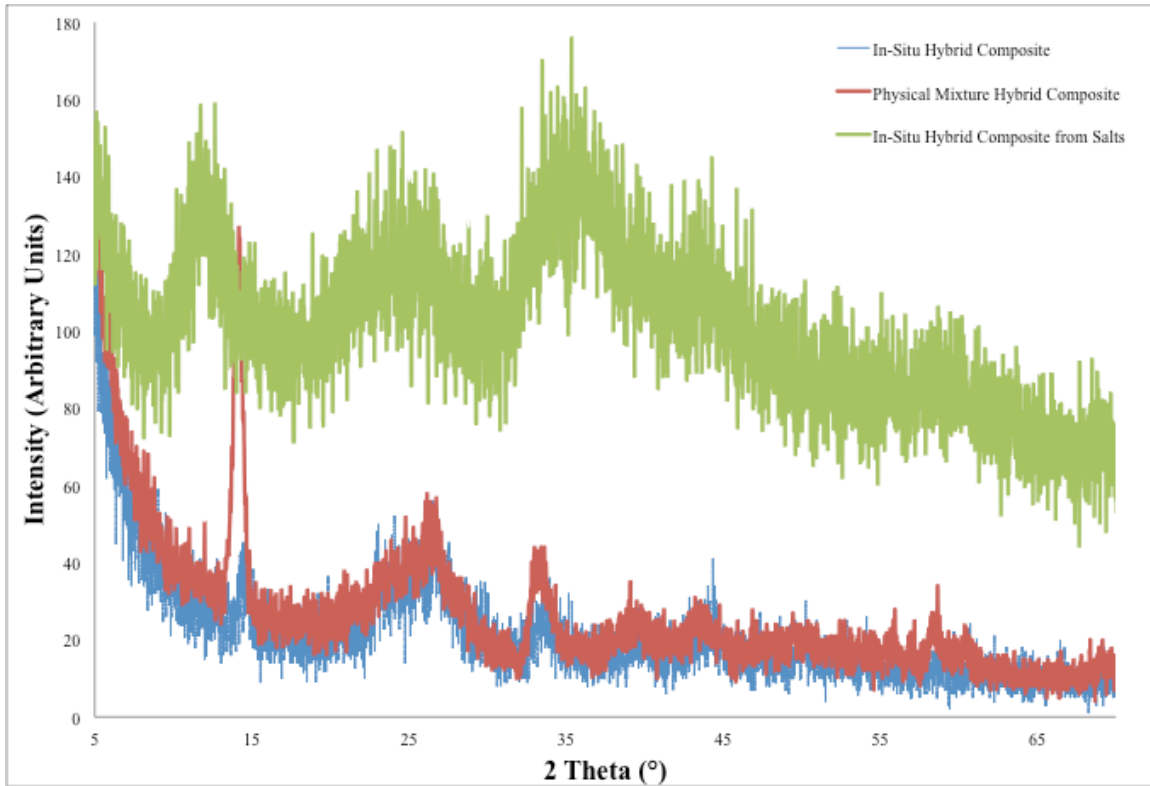


Figure 53. XRD graph of combined methods for producing hybrids.

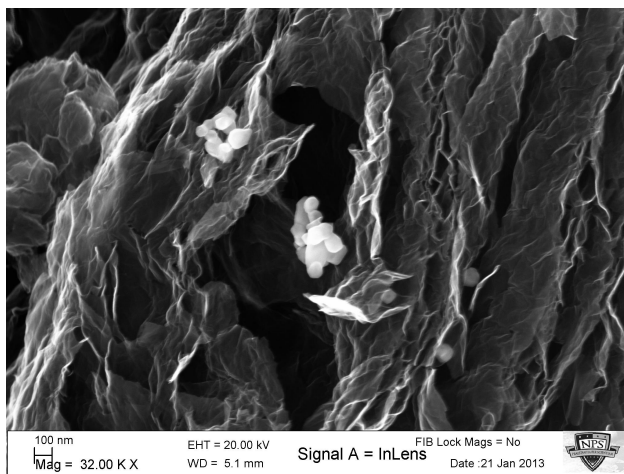


Figure 54. SEM image of physical mixture hybrid.

Figures 54 and 55 demonstrate that the exfoliation of the sheet was able to occur in the sample during the exfoliation process, as well as the dispersion of the IF-WS₂ occurred, with the IF-WS₂ actually located in between the graphene sheets.

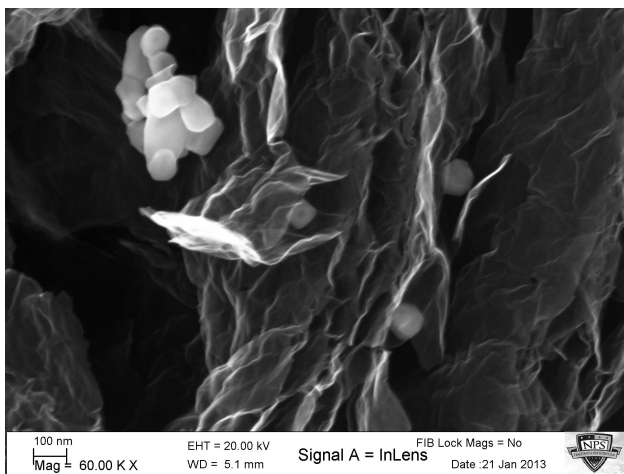


Figure 55. SEM image of physical mixture hybrid to illustrate the IF-WS₂ agglomerates and the placement of the IF-WS₂ between the graphene sheets.

It should be noted that in the above image the IF-WS₂ particles were approximately 100 nanometers in diameter, and they were able to go between a large space in between two graphene sheets. This phase distribution was the one we were

trying to obtain, and represents the achievement of the goal of creating a Graphene/IF-WS₂ hybrid in which both phases are randomly distributed at the nanometer scale.

3. Nanoindentation

After establishing protocols to integrate graphene with IF-WS₂, both by an *in-situ* approach and by physically mixing the components in order to have a random distribution of one phase into the other, samples were tested using a nanoindenter. For reference, individual components, exfoliated graphene (TEGO), plasma produced IF-WS₂, a physical mixture hybrid composite and an *in-situ* hybrid composite at two different loadings, were tested via nanoindentation. For this testing, the hybrid comprised 1% by weight of the total weight to the epoxy used (see Figure 56). Furthermore, for the composite samples the physical mixture was comprised of 1% IF-WS₂ to 99% TEGO, one of the *in-situ* hybrid composites was 1.5% IF-WS₂ to 98.5% TEGO by weight, and the other *in-situ* hybrid composite was .5% IF-WS₂ to 99.5% TEGO by weight. Those values have been summarized in Table 3.

Loading	Graphene	-	WS ₂
Middle	98.5%	-	1.5%
Low	99.5%	-	0.5%
Physical Mix	99%		1%

Table 12. Hybrid Composition by wt %.

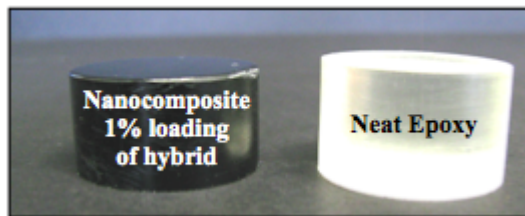


Figure 56. Picture showing an epoxy composite compared to the neat epoxy mounts.

Composites incorporating carbon nanostructures within a polymeric matrix have attracted significant attention due to their high stiffness and strength at relatively low content of carbonaceous material. Most published literature refers to systems in which the carbonaceous material is composed by carbon nanotubes or nanofibers [42]. Although, a major challenge for the success and effective use of such composite materials is to obtain a homogenous dispersion of the filler or granular material within the polymer matrix. The strong intermolecular van der Waals interactions between nanocarbon material parts (i.e., CNTs) along with their large surface area, result in the formation of conglomerates difficult to disperse. Moreover, achieving an acceptable level of adhesion between the nanocarbon phase and the polymer still remains a problem to be solved. Some of the routes followed for composite preparation include: solution mixing [43], melt compounding and *in-situ* polymerization [44].

Given the vast body of literature concerning epoxy resin composites, and the ease to form homogeneous dispersions of solids into the epoxy matrices, this thesis work was performed using such a system. By mixing the required amount of resin with the 1% of nanomaterials by stirring vigorously for two minutes and sonicating for three minutes, homogeneous mixtures were achieved. To this mixture the required amount of hardening agent was added and then stirred vigorously for a period of two minutes, after which the mixture was sonicated for another three minutes until homogeneous. In the case of this research, sonication techniques greatly improved the quality of the dispersion, overcoming the first obstacle normally encountered while generating composites.

Notable from the nanoindentation results, is the fact that the addition of individual components (all in 1% loading) produced a modest increase in the elastic modulus of the composite (see Figures 57 and 58). Exfoliated graphene, TEGO, produced only about 3% increase when compared to IF-WS₂ prepared by plasma routes, which shows a 6% increase. The reason for the different values of individual materials (Graphene vs. IF-WS₂) could be explained from the characteristics of each bonding type and the system components. It is our interpretation that the surface functionalities of graphene, namely oxygen groups in GO were removed to a large extent, by the exfoliation process, leaving carbon sheets of graphene that are difficult to attach by themselves to the polymeric

matrix. In contrast, WS_2 structures could attach through sulfur bonds, to the epoxy resin, a process that has been observed in different sulfur containing species and are the base of vulcanization processes. The larger increase in elastic modulus by 12.23% (3.718 GPa to 4.173 GPa) was observed for the physical mixture hybrid composite. We believe that the individual components were dispersed with more ease than the mixture of the same, aiding the curing process in the epoxy and reflected in the final values for elastic modulus.

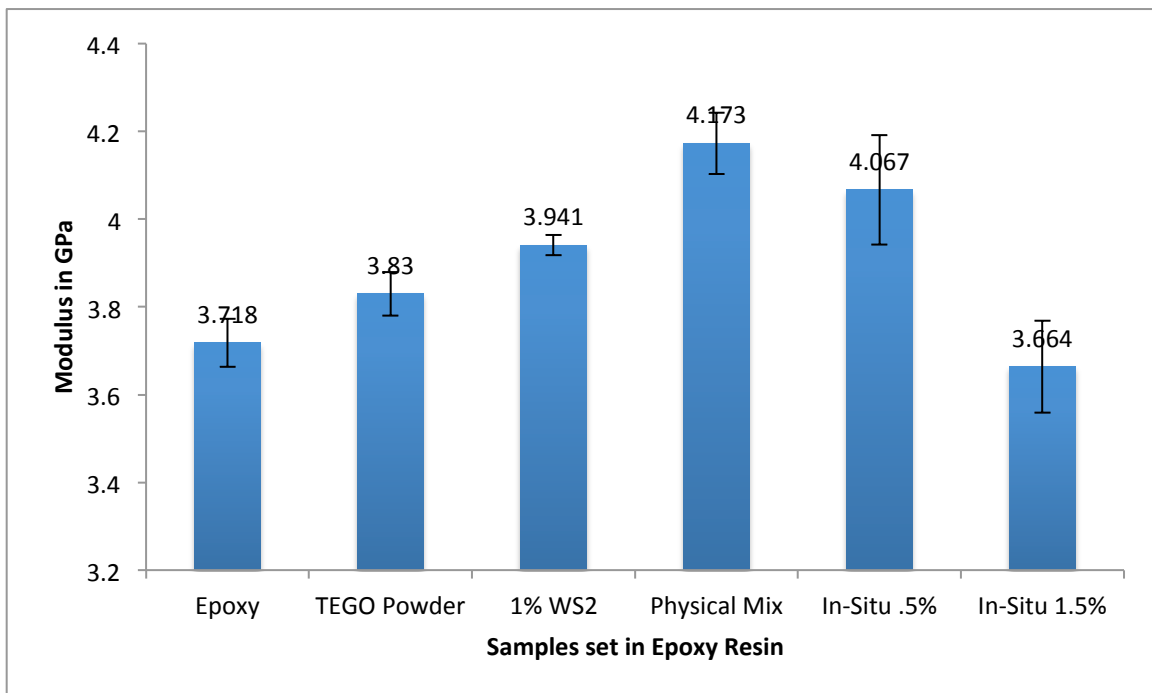


Figure 57. Histogram of elastic modulus computed via nanoindentation.

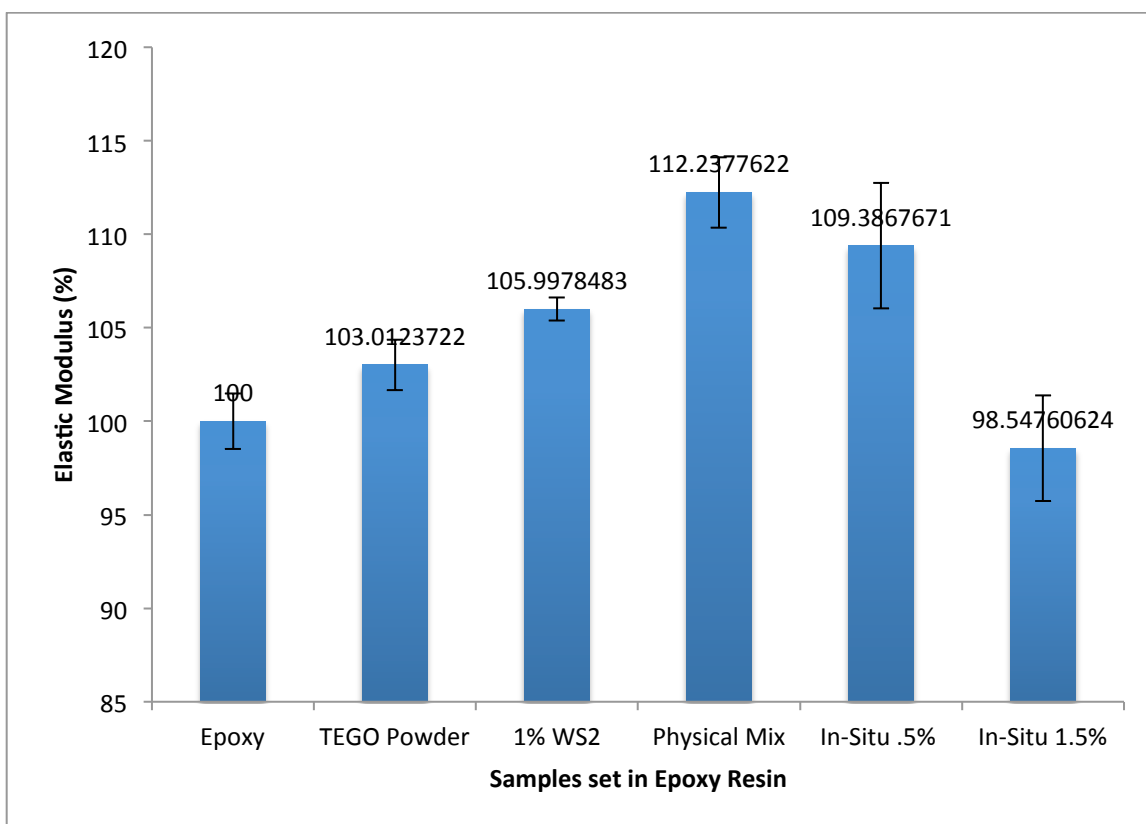


Figure 58. Histogram of normalized elastic modulus computed via nanoindentation.

The greatest increase in mechanical properties for Graphene/IF-WS₂ hybrid included as epoxy composites was observed for hardness values, which can be taken as a measure of how the material presents resistance to plastic deformation or cracking in compression. It can also be translated as a material having better wear properties. When comparing bare epoxy with individual components one could notice that graphene only presents a modest 3% improvement. Such value is much lower than the one observed in carbon nanofiber composites and might be related to a very weak interaction between the graphene layers and the epoxy resin. Moreover, it might also indicate that the dispersion of the fan like structures of graphene are far from ideal and the polymeric matrix did not reach the crevices and the gaps in the structure. Future steps will include the analysis of samples cross section to verify the dispersion of the component. Tungsten disulfide included as IF particles seems to have a improved hardness than graphene as individual component. As mentioned before, the sulfur in the structure is suspected to impose a different interaction and larger likelihood to promote C-S bonding with the matrix.

Exhibiting a 47.27% (0.165 GPa to 0.243 GPa) improvement in the hardness value when compared to bare epoxy, the 0.5% *in-situ* hybrid composite produced the most favorable results (see Figures 59 and 60). When the graphene/WS₂ hybrids' performance in epoxy resins is compared to CNF/IF-WS₂ composites generated by ENS Michael Moberg (also an NPS graduate) [32], the CNF/IF-WS₂ present a higher level of improvement (up to 247% in hardness, 99% in modulus compared to bare epoxy). However, graphene based hybrids might have a better performance when used in a geometry that promotes the free movement of its layers, in a similar fashion than ballistic fibers do (illustrated in Figure 61).

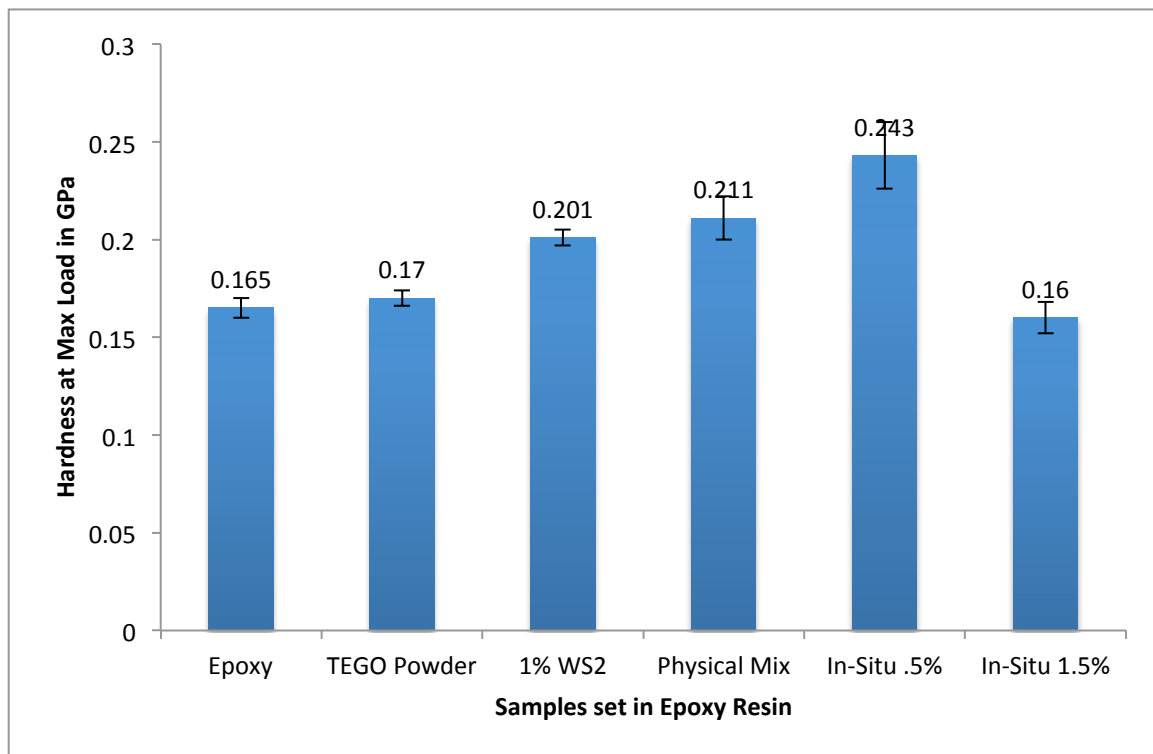


Figure 59. Histogram of hardness computed via nanoindentation.

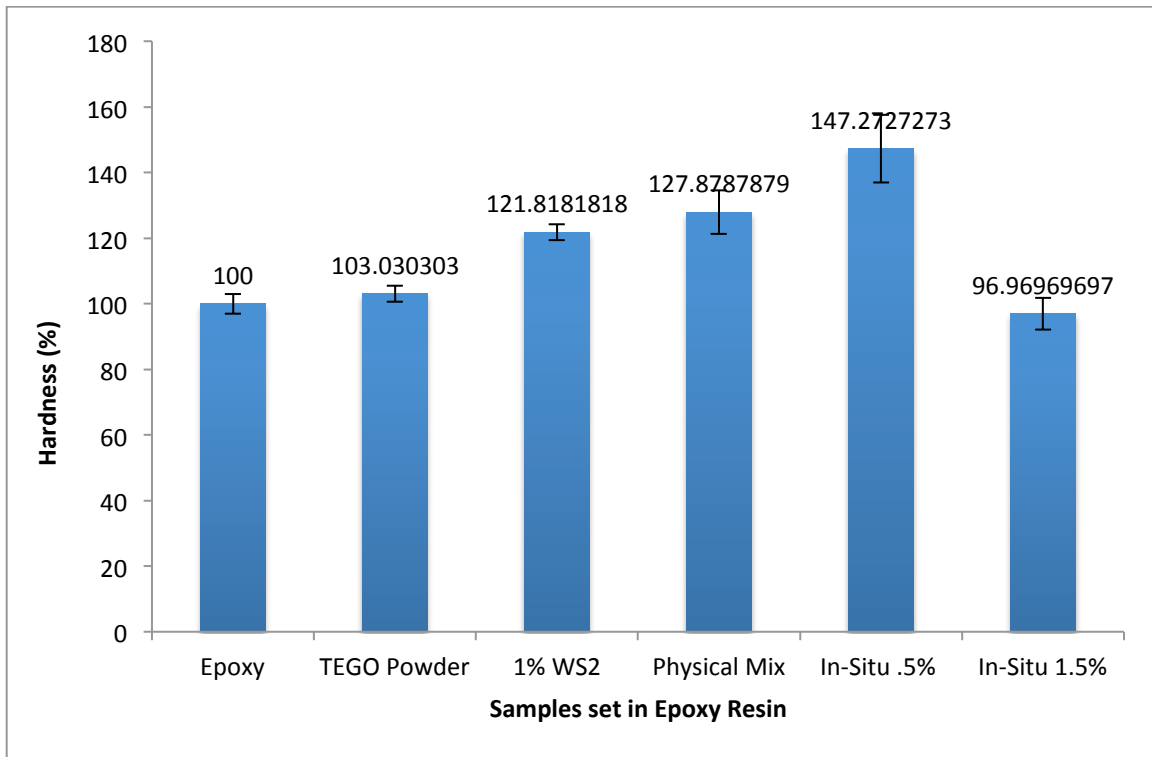


Figure 60. Histogram of normalized hardness computed via nanoindentation.

Regarding mechanisms to dissipate shock waves by graphene/IF-WS₂ hybrids: tests will need to be performed by a different mean to determine coefficients of shock absorption in the hybrid before include in the epoxy matrix to fully foresee the potential of its use as backing material for blunt trauma reduction. The morphology of the graphene sheets produced by GO exfoliation have geometries that could be compared to the ones used in radiation absorption honeycomb structures or other absorbing materials and are related to the ability of the material to deform and regain their shape.



Figure 61. Image showing the impact of a penetrator to a layer of fabric armor (from *Stanford University's AHPCRC*, [online], Accessed 27 May, 2012).

It has been hypothesized that IF-WS₂ mechanisms for energy absorption could be related to the flexibility of the structure [25], since in the absence of a rigid core restrictions and given the hollow core morphology observed, the material will present a spring-like response to an applied shock. The passage of the shock will induce both elastic and plastic deformation within the IF or might also be capable of delaminating the outer layers, leaving most of the particle unchanged. The natural strain observed in the structure, both by XRD and TEM observations, caused by the curvature of the lattice to form cage like structures, will be then released. See Figure 62.

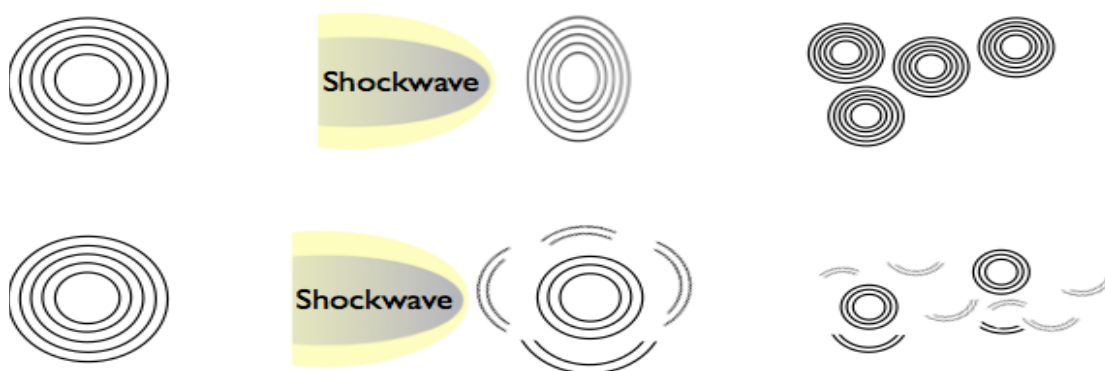


Figure 62. Illustration of shockwave impacting an IF-WS₂ and the associated expected methods of deformation.

THIS PAGE INTENTIONALLY LEFT BLANK

V. CONCLUSIONS

A. Milestones

Making use of plasma based technology and exfoliation of graphitic oxide routes, we were able to generate graphene/IF-WS₂ hybrids. Those were then included in epoxy matrices for selected mechanical properties determination. These novel light-weight composites showed moderate improvements for modulus of elasticity and hardness when compared to base epoxy, validating our hypothesis.

Advantages of the novel methods used to fabricate the hybrids when compared to previous approaches include:

Particles of WS₂ generated from plasma WO₃ present higher crystallinity than the ones produced from salts (NH₄)₂WS₄ and similar to the IF-WS₂ from commercial WO₃. The latter do not completely sulfurize, as some of the oxides remain after the sulfurization step. Plasma generated IF-WS₂ have smaller particle distributions (larger angles (greater than 90°) in polygonal edges, which when fully sulfurized are associated with better mechanical properties. All of the produced IF-WS₂ particles contain hollow cores, as verified with TEM and FIB data, which is also associated with the ability to withstand shock waves.

Graphene produced from exfoliated graphite oxide (GO) is a suitable material to fabricate Graphene/IF-WS₂ hybrids, either as *in-situ* generated nanohybrid or as a physical mixture through the use of solvent and sonication. We used diverse amounts of IF-WS₂ loadings (all with values less than 3%) to produce the composite materials. Only 1% wt of the hybrid in epoxy produced significant changes in modulus and hardness values. Graphene/IF-WS₂ hybrids included in epoxy matrices were created to compare with physical mixtures. We found the physical mixtures produced better dispersion of particles in the graphene honeycomb structures. A small but consistently measurable increase in elastic modulus and hardness was observed for the hybrid composites.

Exhibiting a 47.27% (0.165 GPa to 0.243 GPa) improvement in the hardness value when compared to bare epoxy, the 0.5% *in-situ* graphene/IF-WS₂ hybrid composite

produced the most favorable results. When the graphene/WS₂ hybrids' performance in epoxy resins is compared to CNF/IF-WS₂ composites generated by ENS Michael Moberg (also an NPS graduate) [32], the CNF/IF-WS₂ present a higher level of improvement (up to 247% in hardness, 99% in modulus compared to bare epoxy). However, graphene based hybrids might have a better performance when used in a geometry that promotes the free movement of its layers, in a similar fashion than ballistic fibers do.

These hybrids are currently being tested for their shock absorbing properties—with the possibility to be used as shock absorbing backing layer to reduce effects of blunt trauma.

B. Next Steps

The scaling up of the research involves further testing to determine the materials resistance to shock, now that impact resistance has been established through nanoindentation. The composite Graphene/IF-WS₂ is being produced to provide nanopowder layers between current fabric technologies, while the nanopowder composite is also being mounted in an epoxy matrix to be layered between current fabric technologies. These mounted multi-layer fabric/composite material will be used to undergo shock resistance testing using military rounds.

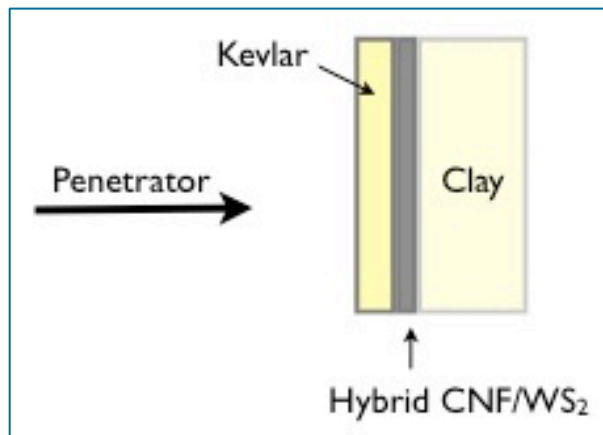


Figure 63. Illustration showing the shock resistance testing for the scaled up material using military rounds.

Following the testing of the fabric/composite material, it will be subjected to post-mortem analysis for the shock/rarefaction-induced plastic deformation, failure surfaces and morphology changes by SEM, TEM, XRD and any surface changes using Brunauer Emmett Teller Method. Through the testing we expect to show that these hybrids will be effective backing layers for the reduction of injuries sustained by our soldiers and sailors from blunt trauma.

THIS PAGE INTENTIONALLY LEFT BLANK

LIST OF REFERENCES

- [1] F. Romero, “A brief history of body armor,” *Times*, April 07, p. 1, 2009.
- [2] Dupont, *Kevlar aramid fiber*, p. 1, 2013.
- [3] N. V. David, X. L. Gao and J. Q. Zheng, “Ballistic resistant body armor: contemporary and prospective materials and related protection mechanisms,” *Applied Mechanics Reviews*, vol. 62, pp. 1–20, 2009.
- [4] M. Grujicic *et al.*, “ballistic-protection performance of carbon-nanotube-doped poly-vinyl-ester-epoxy matrix composite armor reinforced with e-glass fiber mats,” *Materials Science and Engineering A-Structural Materials Properties Microstructure and Processing*, vol. 479, pp. 10–22, 2008.
- [5] P. G. Karandikar, G. Evans and M. K. Aghajanian, “Carbon nanotube (CNT) and carbon fiber reinforced high toughness reaction bonded composites,” *Nanostructured Materials and Nanotechnology*, vol. 28, pp. 53–63, 2008.
- [6] J. H. Lee *et al.*, “Periodic bicontinuous composites for high specific energy absorption,” *Nano Letters*, vol. 12, pp. 4392–4396, 2012.
- [7] Y. Liu *et al.*, “Functionalization of cotton with carbon nanotubes,” *Journal of Materials Chemistry*, vol. 18, pp. 3454–3460, 2008.
- [8] D. C. Marcano *et al.*, “Improved synthesis of graphene oxide,” *American Chemical Society Nano*, vol. 4, pp. 4806–4814, 2010.
- [9] M. Naffakh, A. M. Diez-Pascual and M. A. Gomez-Fatou, “New hybrid nanocomposites containing carbon nanotubes, inorganic fullerene-like WS₂ nanoparticles and poly(ether ether ketone) (PEEK),” *Journal of Materials Chemistry*, vol. 21, pp. 7425–7433, 2011.
- [10] Z. Wang *et al.*, “Ultra-narrow WS₂ nanoribbons encapsulated in carbon nanotubes,” *Journal of Materials Chemistry*, vol. 21, pp. 171–180, 2011.
- [11] D. C. Wei *et al.*, “Synthesis of n-doped graphene by chemical vapor deposition and its electrical properties,” *Nano Letters*, vol. 9, pp. 7, 2009.
- [12] R. Whitby *et al.*, “WS₂ nanotubes containing single-walled carbon nanotube bundles,” *Applied Physics Letters*, vol. 79, pp. 4574–4576, 2001.

- [13] M. Kakran, *Graphene: the new wonder material*, Nov. 10, 2012 [Online]. Available: <http://conferences.theiet.org/ambition/present-world/m-kakran-synopsis.cfm>
- [14] L. Pauling, "The structure of chlorites," *Proc. Nat. Acad. Sci. USA*, vol. 16, pp. 578–582, 1930.
- [15] S. Iijima, "Helical microtubules of graphite carbon," *Nature*, vol. 354, pp. 56–58, 1991.
- [16] H. W. Kroto, et al., "Buckminsterfullerene," *Nature*, vol. 318, pp. 162–163, 1985.
- [17] R. Tenne *et al.*, "Polyhedral and cylindrical structures of tungsten disulphide," *Nature*, vol. 360, pp. 444–445, 1992.
- [18] R. Tenne, "Inorganic fulleren-like structures-ifs." Department of Materials and Interfaces, Weizmann Institute of Science, n.d.
- [19] C. Feng *et al.*, "Synthesis of tungsten disulfide (WS₂) nanoflakes for lithium ion battery applications," *Electrochemistry Communications*, vol. 9, pp. 119–122, 2007.
- [20] R. Tenne, "Doping control for nanotubes," *Nature*, vol. 431, pp. 640–641, 2004.
- [21] H. Yang *et al.*, "Synthesis of inorganic fullerene-like WS₂ nanoparticles and their lubricating performance," *Nanotechnology*, vol. 17, pp. 1512–1519, 2006.
- [22] J. Chen *et al.*, "Synthesis and characterization of WS₂ nanotubes," *Chem. Mater.*, vol. 15, pp. 1012–1019, 2003.
- [23] W. X. Chen, "Characteristics of nested hollow inorganic fullerene-like tungsten disulfide nanoparticles prepared by solid-gas reaction," *Chinese Chemical Letters*, vol. 14.3, pp. 312–315, 2003.
- [24] A. M. Diez-Pascual, M. Naffakh and M. A. Gomez-Fatou, "Mechanical and electrical properties of novel poly(ether ether ketone)/carbon nanotube/inorganic fullerene-like WS₂ hybrid nanocomposites: Experimental Measurements and Theoretical Predictions," *Materials Chemistry and Physics*, vol. 130, pp. 126–133, 2011.
- [25] X. L. Li, G. Jian-Ping and Y. D. Li, "Atmospheric pressure chemical vapor deposition: an alternative route to large-scale MoS₂ and WS₂ inorganic fullerene-like nanostructures and nanoflowers," *Chem. Eur. J.*, vol. 10, pp. 6163–6171, 2004.

- [26] O. Lignier, G. Couturier and J. Salardene, "Growth mechanism of 2H-WS₂ thin films: a similar process to graphitization," *Thin Solid Films*, vol. 338, pp. 75–80, 1999.
- [27] A. Margolin *et al.*, "Study of the growth mechanism of WS₂ nanotubes produced by a fluidized bed reactor," *Journal of Materials Chemistry*, vol. 14, pp. 617–624, 2004.
- [28] H. S. S. R. Matte *et al.*, "MoS₂ and WS₂ analogues of graphene," *Angew. Chem. Int. Ed.*, vol. 49, pp. 4059–4062, 2010.
- [29] M. Tehrani *et al.*, "Synthesis of WS₂ nanostructures from the reaction of WO₃ with CS₂ and mechanical characterization of WS₂ nanotube composites," *Nanotechnology*, vol. 22, pp. 1–10, 2011.
- [30] Y. Zhu *et al.*, "Graphene and graphene oxide: synthesis, properties, and applications," *Advanced Materials*, pp. 1–19, 2010.
- [31] J. Phillips, C. C. Luhrs and M. Richard, "Review: engineering particles using the aerosol-through-plasma method," *IEEE Trans. Plasma Sci*, vol. 37, pp. 726–739, 2009.
- [32] M. J. Moberg, "Carbon fiber and tungsten disulfide nanoscale architectures for armor applications," 2012.
- [33] A. Dato, J. Phillips and M. Frenklach, "Substrate-free gas phase synthesis of graphene sheets," *Nano Letters*, vol. 8, pp. 5, 2008.
- [34] A. D. McAllister *et al.*, "Single sheet functionalized graphene by oxidation and thermal expansion of graphite," *Chem Mater*, vol. 19, pp. 9, 2007.
- [35] M. M. Schniepp *et al.*, "Functionalized single graphene sheets derived from splitting graphite oxide," *Journal of Physical Chemistry B Letters*, vol. 110, pp. 5, 2006.
- [36] H. S. Ju, S. H. Choi and H. L. Lee, "Structures of thermally and chemically reduced graphene," *Material Letters*, vol. 64, pp. 4, 2010.
- [37] S. Wakeland *et al.*, "Production of graphene from graphite oxide using urea as expansion-reduction agent," *Carbon* 48, vol. 0008, pp. 3463–3470, 2010.
- [38] D. R. Dreyer *et al.*, "The chemistry of graphene oxide," *Chemical Society Reviews*, vol. 39, pp. 228–240, 2010.

- [39] R. Tenne, "Inorganic nanotubes and fullerene-like nanoparticles," *Nature*, vol. 1, pp. 103–110, 2006.
- [40] R. Tenne and M. Redlich, "Recent progress in the research of inorganic fullerene-like nanoparticles and inorganic nanotubes," *The Royal Society of Chemistry*, vol. 39, pp. 1423–1434, 2010.
- [41] Y. Q. Zhu *et al.*, "WS₂ and MoS₂ inorganic fullerenes-super shock absorbers at very high pressures," *Advanced Materials*, vol. 17, pp. 1500–1503, 2005.
- [42] Y. T. Sung *et al.*, "Rheological and electrical properties of polycarbonate/multi-walled carbon nanotube composites," *Polymer*, vol. 47, pp. 4434–4439, 2006.
- [43] A. M. Diez-Pascual *et al.*, "Development and characterization of PEEK/carbon nanotube composites," *Carbon*, vol. 47, pp. 3079–3090, 2009.
- [44] H. J. Barraza *et al.*, "Thermoplastic and elastomeric composites prepared by miniemulsion polymerization," *Nano Letters*, vol. 2, pp. 797–802, 2002.
- [45] G. Pharr, W. Oliver and F. Brotzen, "On the generality of the relationship among contact stiffness contact area and elastic modulus during indentation," *Materials Research Society*, vol. 7, no. 3, pp. 613–617, March 1992

INITIAL DISTRIBUTION LIST

1. Defense Technical Information Center
Ft. Belvoir, Virginia
2. Dudley Knox Library
Naval Postgraduate School
Monterey, California
3. Professor Claudia Luhrs
Naval Postgraduate School
Monterey, California